



HAL
open science

Light harvesting hexamolybdenum cluster integrated with the 3D ordered semiconductor inverse opals for optoelectronic property

T.K.N. Nguyen, Fabien Grasset, S. Cordier, N. Dumait, S. Ishii, H. Fudouzi, T. Uchikoshi

► To cite this version:

T.K.N. Nguyen, Fabien Grasset, S. Cordier, N. Dumait, S. Ishii, et al.. Light harvesting hexamolybdenum cluster integrated with the 3D ordered semiconductor inverse opals for optoelectronic property. *Materials Today Chemistry*, 2023, 27, pp.101351. <10.1016/j.mtchem.2022.101351>. <hal-03927650>

HAL Id: hal-03927650

<https://hal.science/hal-03927650v1>

Submitted on 10 Jan 2023

HAL is a multi-disciplinary open access archive for the deposit and dissemination of scientific research documents, whether they are published or not. The documents may come from teaching and research institutions in France or abroad, or from public or private research centers.

L'archive ouverte pluridisciplinaire HAL, est destinée au dépôt et à la diffusion de documents scientifiques de niveau recherche, publiés ou non, émanant des établissements d'enseignement et de recherche français ou étrangers, des laboratoires publics ou privés.



HAL Authorization

1 **Light harvesting hexamolybdenum cluster integrated with the 3D ordered**
2 **semiconductor inverse opals for optoelectronic property**

3 Thi Kim Ngan Nguyen¹, Fabien Grasset^{2,3}, Stéphane Cordier³, Noée Dumait³, Satoshi
4 Ishii⁴, Hiroshi Fudouzi⁵, Tetsuo Uchikoshi^{2,5}

5 ¹International Center for Young Scientists, Global Networking Division, National
6 Institute for Materials Science, 1-2-1 Sengen, Tsukuba, Ibaraki 305-0044, Japan

7 ²CNRS–Saint-Gobain–NIMS, IRL3629, Laboratory for Innovative Key Materials and
8 Structures, National Institute for Materials Science, 1-1 Namiki, Tsukuba, Ibaraki 305-
9 0044, Japan

10 ³Univ. Rennes-CNRS-Institut des Sciences Chimiques de Rennes, UMR6226, 35000
11 Rennes, France

12 ⁴Photonics Nano-Engineering Group, International Center for Materials
13 Nanoarchitectonics, National Institute for Materials Science, 1-1 Namiki, Tsukuba,
14 Ibaraki 305-0044, Japan

15 ⁵Research Center for Functional Materials, National Institute for Materials Science, 1-2-
16 1 Sengen, Tsukuba, Ibaraki 305-0044, Japan

17 Corresponding author: Thi Kim Ngan NGUYEN

18 Full postal address: International Center for Young Scientists, National Institute for
19 Materials Science (NIMS), 1-2-1 Sengen, Tsukuba, Ibaraki 305-0047, Japan

20 E-Mail address: NGUYEN.Thikimngan@nims.go.jp

21 **ABSTRACT**

22 Solar energy-harvesting materials have significantly contributed to the development of
23 energy-saving applications for several decades. We have mainly used a new concept
24 composed of the electrophoretic deposition technique and photonic crystal structural
25 engineering to understand the tunable light-absorption and electronic conduction
26 properties. A hexamolybdenum cluster compound (denoted as the Mo₆ cluster) was

27 successfully functionalized on a tin pyrophosphate semiconductor integrated within an
28 inverse opal photonic crystal. The size of the periodical pores, surface modification, and
29 chemical composition of the infiltration material of the inverse opal film have been
30 investigated to control the photonic bandgap in the visible range and the efficiency of the
31 deposited Mo₆ cluster. The photoactive Mo₆ clusters act as a visible light harvester and
32 generate an efficient photo-induced current upon light absorption that is enhanced by a
33 slow photon effect occurring at the photonic stopband edges. The electron and proton are
34 transferred in the inorganic-organic network via hydrogen bonds by a hopping
35 mechanism to generate a rapid photoconductivity response during light irradiation.
36 Specific attention focused on the role of humidity and temperature regarding the
37 reproducibility of the experiments and the photosensitivity of the nanocomposite. The
38 suitable tunable photo-induced conduction property in organic-inorganic materials opens
39 a new opportunity for the applicability of cluster-based compounds in visible
40 optoelectronic devices.

41 **KEYWORDS:** hexamolybdenum atom cluster, optical material, 3D inverse opal
42 structure, optoelectronic, visible light harvesting, surface chemistry

43 1. INTRODUCTION

44 Considering the serious global warming problem, the discovery of a solar energy-
45 converting material in the Vis-NIR domain for optoelectronic devices, such as
46 photodetectors, light emission devices, sensors, and dye-sensitized solar cells, has
47 occurred [1-5]. Among the nanoarchitecture nanomaterials, the $[M_6L^i_8L^a_6]^{n-}$ cluster unit,
48 composed of a central Mo₆ cluster, eight inner ligands at the face-capping position ($L^i =$
49 halogen or chalcogen; i for inner), and six apical ligands at the terminal positions ($L^a =$
50 halogen, OH⁻, H₂O, N₃, OCOC_nH_{2n+1}, etc; a for apical.), has become attractive due to the
51 delocalization of the valence electrons on the metal centers for producing interesting
52 photochemical and redox properties [6-7]. These metal atom clusters (MCs) exhibit
53 luminescence properties combined with high-quantum yields, a large Stoke shift for
54 preventing absorption loss, strong absorption in the ultraviolet (UV)-Vis domain,
55 photostability at room temperature, and facile processing. These advanced properties
56 have been utilized in the design of optical-related devices, phosphorescent nanocluster

57 emitters, saving-energy devices, photodetectors, photoelectrodes for DSSC, and
58 photocatalytic electrodes for water splitting [8-14]. In addition, the tunable photo-induced
59 electronic property of the MC with functional semiconductors has been recently
60 investigated which will be a fascinating property for optoelectronic devices [15-17].
61 Renaud et al. explored the potential of Mo₆ clusters as new nontoxic and stable inorganic
62 sensitizers with amphoteric properties for light-emitting photoelectrodes that were
63 achieved and integrated into solar cell devices [13]. The influence of light on the electrical
64 properties of ionic conductors, the so-called opto-ionic property, around room
65 temperature has become a hot topic, especially ionic conduction, which is crucial and
66 very promising. A UV-Vis photodetector based on Mo₆ clusters embedded in a protonic
67 conducting 2D material was demonstrated by Nguyen et al. It revealed that the
68 reproducibility and stabilization of the ionic photocurrent response were verified upon
69 light excitation at 540 nm which linearly depends on the relative humidity and
70 temperature [12]. However, potential applications based on the cluster face many
71 challenges due to the difficult control of a mono-dispersed cluster distribution, thermal
72 and chemical stability, and production on a large scale. The combination of the nano-
73 sized atom cluster with functional supporting materials; i.e., semiconductor, polymer, or
74 hybrid, becomes an interesting solution in order to enhance the atom cluster's weakness.
75 However, the charge transport between the cluster and the semiconductor is an important
76 point to develop tunable photo-induced conducting properties.

77 Recently, the enhancement of the efficient photoconductivity response has been studied
78 for visible light-harvesting materials, such as cadmium zinc telluride (CZT), cobalt-doped
79 zinc ferrite oxide, or the use of specialized techniques, such as scalable photonic platforms
80 based on silicon, and the band engineering of the TiO₂/Si heterojunction [18-21]. As is
81 known, artificial photonic crystal inverse opal (IO) structures can propagate the angle-
82 dependent refractive light by using the periodic variation in the dielectric contrast or
83 reflective index contrast within a crystal [22-23]. Light scattered or/and diffracted from
84 the different surfaces will produce a full or partial photonic bandgap (PBG). This PBG
85 and its manipulation ability could be deeply understood in researching different
86 infiltration material precursors, various synthesis routes, and structural depending
87 applications. The interesting advantages of this structure are subsequent inhibition of the

88 spontaneous emission, and the possibility to localize and enhance the emission or
89 reflection of light. Moreover, in the 3D inverse opal photonic crystal, slow photon-
90 induced light absorption is considered more than the photonic bandgap-induced light
91 reflection for enhancing the generation of an electron-hole pair upon illumination [24].
92 The 3D-ordered porous structure has been potentially developed for photodetectors,
93 photoelectrodes for water splittings, photocatalysts, oxygen or hydrogen evolution
94 reactions, and light-trapping parts for dye-sensitive solar cells [25-31]. In addition, the
95 ordered porous inverse opal supplies a large area for the active site, a promising loading
96 possibility of the active materials, necessary transmittance for the transparent conducting
97 substrate, controllable photon absorption, etc. [29, 30]. The first goal of this study is to
98 use the inverse opal photonic crystal to enhance the visible light absorption of the Mo₆
99 cluster.

100 The metal atom cluster exhibits an excellent photoactive property upon UV-Vis light
101 illumination to generate electron-hole pairs, however, the excited electron will
102 immediately recombine with the hole without transporting in the network. The second
103 goal of this study is to select metal oxide semiconductors exhibiting high electron and
104 ionic conductivities as a carrier for producing a high photoconductivity response. As is
105 known, proton metallic phosphate conductors (MP₂O₇; M = Sn, Al, Mg, In, etc.) are
106 potential candidates which have been studied in electrochemical device, such as
107 intermediate-temperature proton conductors for fuel cells, batteries, gas sensors, NIR
108 phosphor-converted light-emitting diode, etc. [32-38]. The protonic and electron-hole
109 conductivity of SnP₂O₇ essentially occurs in the bulk material rather than on the surface
110 and is influenced by the structural characteristic, single cubic crystal or amorphous one
111 [39, 40].

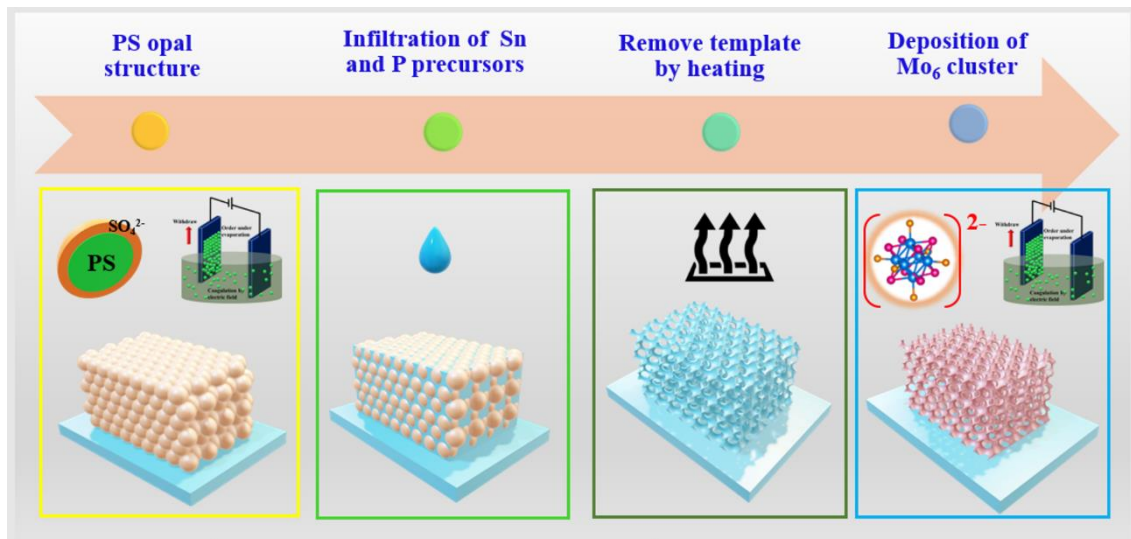
112 Until now, only one idea based on a silica opal photonic crystal and atom metal cluster
113 has been reported with an increase in the emission intensity in the energy range of the
114 passband [41]. For the first time, the SnP₂O₇ proton conductor integrated with an inverse
115 opal photonic crystal functionalized with the photoactive Mo₆ cluster iodide
116 ($\{[Mo_6I_8]I_4[H_2O]_2\}_y \cdot H_2O$) was successfully fabricated by using electrophoretic
117 deposition (EPD), a short-time consuming and efficient technique. The Mo₆ iodide cluster

118 compound, $\text{Cs}_2[\{\text{Mo}_6\text{I}_8\}\text{I}_6]$ (noted CMI), was selected as the cluster precursor due to its
119 strong absorption in the visible light range and photostability under long irradiation [42].
120 The hydrophilic surface modification of the SnP_2O_7 inverse opal film by using citric acid
121 also enhanced the loading concentration of the Mo_6 cluster. The enhancement of the
122 visible light absorption of the Mo_6 cluster was obtained which is a result of the slow
123 photon effect at the PBG edges due to the inverse opal structure. The optimizations of the
124 pore size and ordered porous structure could control the PBG position in order to enhance
125 the photonic energy absorption in the desired wavelength region. The photo-induced
126 current phenomenon was investigated by the photoconductive response generated by AC
127 and DC electric field generators upon light irradiation. The photoconductivity response
128 upon the visible light irradiation from 400 to 580 nm is linearly dependent on temperature
129 and humidity. This concept provided many interesting characteristics which are relevant
130 for designing environmental sensors, a photodiode for a solar cell, or a photodetector.

131 **2. EXPERIMENTAL**

132 **2.1 Preparation of SnP_2O_7 IO films and citric acid-modified SnP_2O_7 IO films**

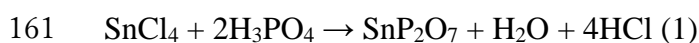
133 **Figure 1** shows a schematic diagram of the simple methods to prepare the SnP_2O_7 IO
134 films. Aqueous solutions containing 8 wt% of monodispersed polystyrene (PS) beads
135 were prepared by the standard emulsion polymerization method [43]. The average sizes
136 (240, 288, and 308 nm) of the PS beads were measured from a scanning electron
137 microscope image. The anodic EPD was used to fabricate the PS-based photonic crystal
138 film with the periodic arranged face-centered cubic lattice. The simple EPD system
139 included two electrodes; i.e., indium tin oxide-coated glass (ITO) (Geomatec Co., Ltd.,
140 Tokyo, Japan; 6.15-7.27 Ohm/sq) with a surface area of $2 \times 3 \text{ cm}^2$ treated in ethanol and
141 stainless steel with a surface area of $2 \times 3 \text{ cm}^2$ treated in ethanol. The distance between the
142 electrodes was fixed at 0.5 cm. The electrodes were connected to a Source Meter
143 (Keithley Model 2400, Ohio, USA) as an electric field generator. The aqueous 8wt% PS
144 solution was diluted by ethanol (99.5%, Nacalai Tesque Co., Ltd.) at the volume ratio of
145 15/85 which is an optimized ratio to obtain a good periodic structure⁴⁴. The EPD opal
146 films were optimally prepared at 10 or 12 V for 1 minute.



147

148 Figure 1. Schematic diagram of the fabrication process of Mo₆ cluster-deposited SnP₂O₇
 149 IO nanostructure using a PS-bead template and electrophoretic deposition (EPD).

150 The precursor solutions for the infiltration process were prepared by dissolving tin
 151 tetrachloride (SnCl₄·5H₂O, 98%, Nacalai Tesque Co., Ltd.) into ethanol: H₂O (volume
 152 ratio of 10:1) at the concentration of 10%. The molar ratio between P (0.5 ml) from
 153 phosphoric acid (H₃PO₄, 85%, Nacalai Tesque Co., Ltd.) and Sn precursors (1 g) was 2.6.
 154 The mixture was stirred for 3h under ambient conditions. Five drops of the solution
 155 mixture were then infiltrated into the PS-based photonic crystal film with an area of 5
 156 cm², then slowly dried for 24 h. The SnP₂O₇ IO film was then fabricated by a thermal
 157 treatment program including 2 steps; i.e., fast heating to temperature T1 (500, 550, or
 158 600°C) and slow heating from temperature T1 to temperature T2 (550, 600, or 650°C) for
 159 reducing cracking because of complete decomposition of the PS. The performance of
 160 SnP₂O₇ is illustrated following reaction (1) at high temperatures.



162 The porous SnP₂O₇ IO film was then immersed in citric acid (98%, FUJIFILM Wako
 163 Pure Chemical Corporation) with a concentration of 52 mM for 10 minutes at 90°C, then
 164 heated at 100°C for 24 h in air. The acid-modified SnP₂O₇ IO film was stored at 50°C in
 165 air for the next fabrication process.

166 **2.2 Preparation of the Mo₆ cluster-deposited SnP₂O₇ IO films**

167 The hexamolybdenum cluster compound $Cs_2[\{Mo_6I_8\}I_6]$ was synthesized by the
168 reaction of CsI (Alfa Aesar 99.9 %) and MoI_2 at a high temperature ($700^\circ C$) following
169 the procedure reported in a previous study [6]. The CMI powder was dissolved in acetone
170 at the concentration of 1g/L by ultrasonication for 1h, then magnetic stirring for 72 h. The
171 use of EPD to deposit the Mo_6 cluster in the porous SnP_2O_7 IO films was optimally
172 studied at a voltage of 15 V and a deposition time of 2 minutes with a deposition area of
173 5 cm^2 . The obtained films were dried at $100^\circ C$ for 24 h to eliminate the residual solvent
174 before the characterization and photocurrent response measurements. An abbreviated
175 representation of the sample is SnPO IO_xca-MI, where ‘SnPO’ is SnP_2O_7 , ‘x’ is the PS
176 bead size (240, 288, 308 nm), ‘ca’ is citric acid, and the ‘MI’ is the hexamolybdenum
177 iodine cluster.

178 **2.3 Measurement of photocurrent response**

179 A cell containing ITO glass coated by SnPO-IO_x, SnPO-IO_xca, SnPO-IO_xca-MI films (x
180 = 240, 288, and 308 nm, the average size of PS bead) and a blank ITO glass with a
181 measured area of $1.2 \times 2\text{ cm}^2$ connected to a micrometer. The film thickness was measured
182 by a scanning electron microscope. The different UV-Vis light illuminations were
183 generated by a 300 W compact Xenon light source (MAX-303, Asahi Spectra Co., Ltd.).
184 A monochromator combined with an optical filter (transmittance ~ 80 %) was used to
185 generate monochromatic light with a bandwidth of 10 nm, centered respectively on 350,
186 370, 410, 440, 540, and 580 nm. The real intensity of the photon energy arriving at the
187 surface of the material film corresponded to almost 80% in the UV-Vis light range (350
188 nm – 600 nm) as revealed by the manufacturer. A source meter (VSP300, Potentiostat,
189 BioLogic) was used to measure the DC photocurrent response of the films at a bias of 0.5
190 V with active area of 2.4 cm^2 . The AC conductivity of the films was measured by a 1260A
191 impedance analyzer (Solartron analytical, AMETEK Scientific Instruments) at a bias of
192 500 mV in the frequency range between 10^1 Hz and 10^7 Hz . All measurements were
193 performed under controlled environmental conditions. The electrical conductivity was
194 expressed by the following **Eq. 1**:

$$195 \quad \sigma = I / (R.A) \quad (1)$$

196 where σ is the electrical conductivity, l is the thickness of the film, A is the area of the
197 sample ($1 \times 1 \text{ cm}^2$), and R is the total resistance measured by Electrochemical Impedance
198 Spectroscopy (EIS).

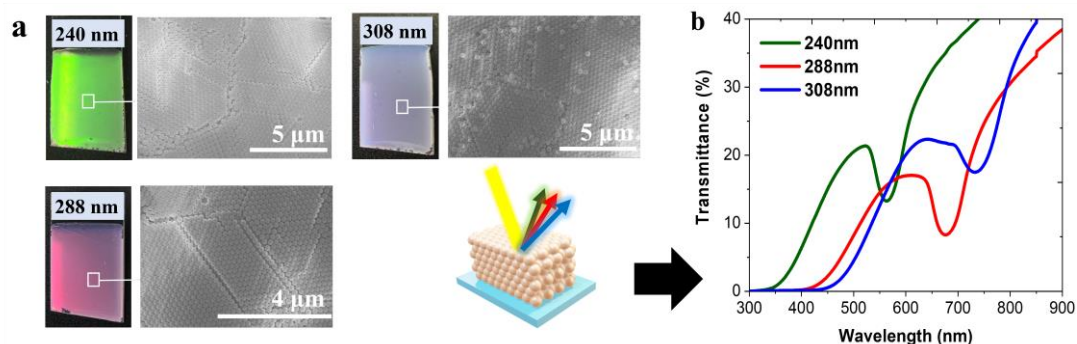
199 **2.4 Characterization**

200 The morphology characteristics were analyzed by field emission scanning electron
201 microscopy (FE-SEM, SU8000, Hitachi High-Technologies Corp.) at 10 kV coupled with
202 an energy-dispersive X-ray (EDX) analysis device. High-resolution (HR) observations of
203 the powder were performed by an HR-transmission electron microscope (HR-TEM)
204 (JEOL JEM 2100F) equipped with an EDX analysis device. The X-ray powder diffraction
205 (XRD) patterns were recorded at room temperature at the 2-theta angle in the range of
206 10° and 60° using a SmartLab diffractometer (RIGAKU, 40 kV and 30 mA) with Cu $K\alpha$
207 radiation ($\lambda = 1.54 \text{ \AA}$), a step size of 0.02° and a scan speed of $1^\circ/\text{min}$. Le Bail fittings
208 were performed using the FullProf program included in the WinPLOTR software [44,
209 45]. The zero-point shift, asymmetry parameters, lattice parameters, and β angle were
210 systematically refined, and the background contribution was manually estimated (**Tab.**
211 **SI1**). The typical chemical vibration of the powder was recorded by Fourier transform
212 infrared spectroscopy (FTIR) (Thermo Scientific Nicolet 4700) in the wavenumber range
213 from 4000 to 400 cm^{-1} using a KBr pellet. The transmittance spectra of the IO films were
214 measured by UV-Vis-NIR spectroscopy (V570, Jasco Corp.) in the wavelength range of
215 200 to 2000 nm at the scan rate of $400 \text{ nm}/\text{min}$. The specular reflectance spectra of the
216 films were measured at the incidence angle of 5 degrees in the wavelength range of 200
217 to 2000 nm by using a UV-Vis-NIR spectrophotometer (Solidspec-3700, Shimadzu
218 Corp.). The luminescent emitting spectra of the films were measured by high-
219 performance fluorescence spectroscopy (JASCO FP8500) connected to a Xenon lamp at
220 the scan rate of $500 \text{ nm}/\text{min}$. The electron binding energy spectra were measured by X-
221 ray photoelectron spectroscopy (XPS) (PHI Quantera SXM (ULVAC-PHI)) using Al $K\alpha$
222 radiation at 20 kV and 5 mA and taken-off angle of 45° . All the binding energies were
223 calibrated concerning the C 1s peak of the adventitious carbon at 285 eV .

224 **3. RESULTS AND DISCUSSION**

225 3.1 Characterization of SnP₂O₇ IO film

226 Recently, the growth of photonic crystals by colloidal assembly routes has been
227 particularly done but their potential in real-world applications still faces many challenges.
228 The difficulties in controlling the external forces of suspension, solvent evaporation rate,
229 withdrawal rate, and template concentration inhibited obtaining the chemical and thermal
230 stability and well-ordered 3D porous structure [22]. EPD is a good technique that shows
231 the flexibility of the substrate sizes and templates, short-time consumption, and uniform
232 structure in comparison to the conventional methods [46]. FE-SEM images from **Fig. 2a**
233 show the surface characteristic of the crystal opal films that were successfully fabricated
234 using the anodic EPD at 10 V for 1 minute. The PS beads with the average sizes of 240
235 nm, 288 nm, and 308 nm were arranged to form well-ordered hexagonally packed
236 photonic crystals that result in reflectance of green, red, and slight red colors as seen in
237 the next photographs. The cross-section images of the films also showed good
238 organization in a face-centered cubic (fcc) structure. The thickness of the different-sized
239 opal films was recorded in the range of 5 to 10 μm (**Fig. S11**) depending on the PS bead
240 size with similar EPD parameters. The optical and photonic bandgaps were based on the
241 UV-Vis transmittance spectra. The transmittance spectra from **Fig. 2b** show specific
242 peaks centered at wavelengths of 563, 677, and 732 nm which indicated the partial
243 photonic band gaps (PBGs) of the opal films corresponding to the 240, 288, and 308 nm-
244 sized PS-bead templates, respectively. The PS spheres are well known without absorption
245 in the blue/violet range. It means that the transmittance at 0 in this range comes from the
246 scattering by the polystyrene spheres. For a larger PS bead size, the scattering appears
247 stronger.
248



249
 250 Figure 2. (a) Photographs of observed color and FE-SEM images of the opal films
 251 prepared by EPD (10 V, 1 minute) using different PS-bead sizes. (b) UV-Vis
 252 transmittance spectra and schematic image of the opal films.

253 For the first time, the SnP_2O_7 inverse opal structure was directly prepared by using the tin
 254 chloride precursor and phosphoric acid with the initial P: Sn molar ratio of 2.6. In this
 255 study, an annealing critical temperature of 600°C was effective to produce the cubic
 256 SnP_2O_7 structure and ordered porous inverse opal structure for the PBGs. The major
 257 reflections in the XRD pattern of the referenced SnP_2O_7 powder synthesized under the
 258 same conditions can be observed at specific 2-theta angles centered at 19.4° (111), 22.4°
 259 (200), 31.8° (200), 37.6° (311), 50.1° (331), 51.5° (420), and 56.8° (422) (**Fig. SI2**). A Le
 260 Bail refinement of the whole samples has been performed and reasonably reliable factors
 261 have been obtained to confirm a space group of cubic $P a-3$ ($a = b = c$, $\beta \approx 90^\circ$) (**Tab.**
 262 **SI1**). A similar pattern was verified for the SnP_2O_7 inverse opal film (SnPO-IO_{288}) with a
 263 weak intensity of crystallinity because of the porous structure (**Fig. 3a**). SnP_2O_7 has a
 264 cubic structure that shows corner-sharing SnO_6 octahedra and PO_4 tetrahedra containing
 265 the oxygen lattice ion on the surface as seen in **Fig. 3b** [47]. The FT-IR spectrum provides
 266 evidence for the symmetric and asymmetric stretching vibrations of the P-O bonds of the
 267 PO_4 groups at the wavenumbers of 1120 cm^{-1} and 960 cm^{-1} (**Fig. 3b**). The vibration band
 268 assigned to the Sn-O bonds was recorded at 498 cm^{-1} . This characteristic peak is in
 269 agreement with previous reports [48].

270 The UV-Vis transmittance spectra from **Fig. 3c** and **Fig. SI3** show the optical and PBGs
 271 of the SnPO-IO_x ($x = 240, 288, 308$) films annealed at different temperatures and
 272 ethanol/ H_2O volume ratios fixed at 10/1. The SnP_2O_7 powder almost shows a low

273 transmittance under 300 nm due to its absorbance in this range. The initial molar ratio of
274 P: Sn is more than 2 and the heat-treating temperature is higher than 500°C which should
275 be applied to definitely obtain the single cubic phase structure of SnP₂O₇ [49]. By the
276 thermal treatment up to 550°C, the SnP₂O₇ phase is performed and the IO film starts to
277 form PBGs but their width is broad and asymmetric (**Fig. S13**). This can be a reason for
278 the impurity of the SnO₂ phase which is not completely transferred to SnP₂O₇ [49]. As is
279 known, the existence of the SnO₂ impurity with a high refractive index can expand the
280 width of the stopband peak. However, at treatment temperatures up to 600°C, the SnP₂O₇
281 IO films definitely show symmetrical PBGs at the wavelengths of 379, 457, and 502 nm,
282 respectively, originating from the 240, 288, and 308 nm-sized PS beads (**Fig. 3c**).
283 Although the single cubic phase structure of SnP₂O₇ was definitely created at 650°C, the
284 high-heating temperature can create much cracking and then destroy the ordered
285 macropore structure. The low transmittance around the stopband positions in **Fig. 3c**
286 (upper) possibly comes from the reflection, scattering, and refraction of the light caused
287 by the inverse opal film. In order to clearly identify these inverse opal PBGs originating
288 from the contribution of reflective light, the spectacular reflectance spectra were obtained
289 at an incident angle of 5 degrees that show similar stopband peaks with a reflective light
290 percentage lower than 15% (**Fig. 3c** under).

291 From **Fig. 3d**, these photographs of the SnPO-IO_x (x= 240, 288, 308) films having pore
292 sizes of about 223, 267, and 294 nm, respectively, are in agreement with the reflectance
293 of the visual violet (379 nm), blue (457 nm), and cyan (502 nm) color (**Fig. 3c** under).
294 The obtained pore size was reduced from 5 to 7 % compared to the initial size of the PS
295 bead as seen in the FE-SEM image. It can be influenced by the shrinkage of PS during
296 the thermal treatment before the SnP₂O₇ crystal was formed. In addition, the low
297 shrinkage also indicated a high SnP₂O₇ condensate. On the other hand, the thickness of
298 the IO film was reduced by less than 10% from 5 to 10 μm while retaining the periodic
299 structure (**Fig. 3d**). The role of water in this step contributes to the association of the Sn
300 precursor that supports their transport in the voids between the PS beads. The pore size
301 and inverse opal structure were confirmed in the STEM images (**Figs. 3e**). The elemental
302 composition of tin pyrophosphate was confirmed to contain O, Sn, and P from the STEM-
303 EDX mapping (**Fig. 3f**). By using the EPD technique, a SnP₂O₇ inverse opal photonic

304 crystal film showing the typical PBG was efficiently prepared in a short time, with a
305 flexible thickness and active area on the TCO substrate. The thermal treatments at
306 temperature T1 of 550°C and temperature T2 of 600°C with different heating rates were
307 fixed to efficiently fabricate the SnPO-IO_x (x = 240, 288, 308) films for the next steps.

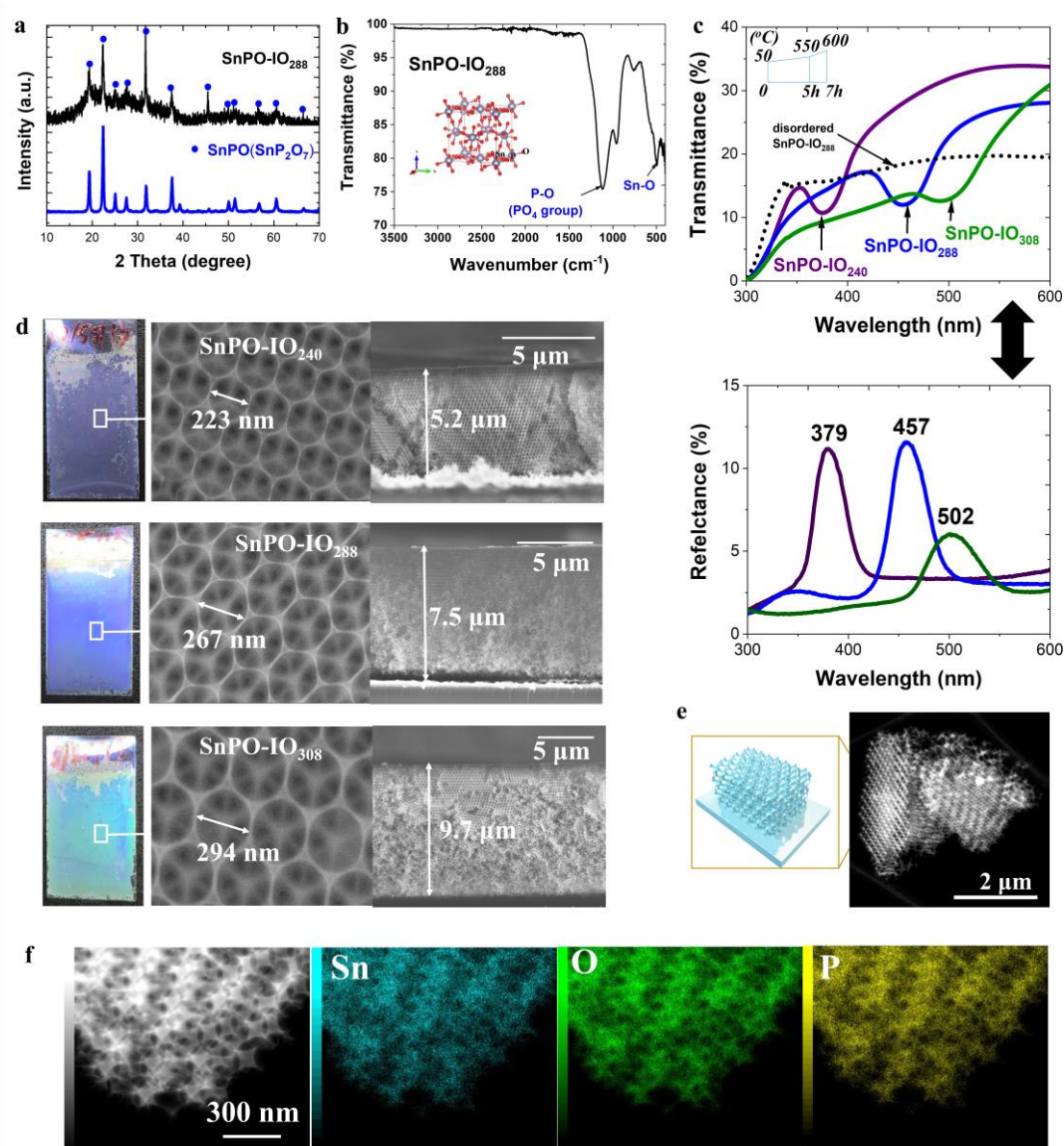
308

309 The approximate stopband position of the inverse opal can be calculated by a modification
310 of Bragg's law taking into account Snell's law of refraction that is expressed in **Eq. 2**
311 [50]:

$$312 \quad \lambda_{\max} = 2D \sqrt{\frac{2}{3} \sqrt{fn_1^2 + (1-f)n_2^2} - \sin^2\theta} \quad (2)$$

313 Where, λ is the stopband position for the first-order Bragg diffraction, D is the PS bead
314 size of the PhCs or pore size of IO, $n_1 = 1$ for air and $n_2 = 1.59$ for PS or $n_1 = 1$ for air and
315 $n_2 \sim 1.65$ for SnP₂O₇ are the refractive indices, and θ is the incidence angle of the light
316 which is 5° in this measurement. Depending on the face-centered cubic (fcc) structure of
317 the photonic crystals, the volume percentage (f) of the air and PS is 0.26 and 0.76,
318 respectively. Based on **Eq.2**, the PS bead sizes of 240, 288, and 308 nm sizes confirmed
319 by the FE-SEM images were used to calculate the PBGs which result in the wavelengths
320 of 571, 685, and 732 nm, respectively. However, the experimental PBGs resulted in a
321 small difference which was taken at 563, 677, and 732 nm as seen in **Table SI2**. The
322 volume fraction of air was calculated from the measured data as more than 0.26 which is
323 taken at the average fraction of 0.36 ± 0.02 . The performance of the well-organized face-
324 centered cubic structure is not completely preferred for a small PS bead size. In the case
325 of the inverse opal structure, refractive indices of 1.65 for SnP₂O₇, the measured pore
326 diameters (223, 267, and 294 nm), and stopband positions (379, 457 and 502 nm) were
327 used to calculate the volume fraction of SnP₂O₇ based on **Eq. 2 (Table SI2)**. It can be
328 seen that the filling factors (f) of air in the SnP₂O₇ inverse opals almost reached more than
329 94%. As the result, the solid filling fractions of the inverse opal skeleton are 5, 6, and 6
330 % for the SnPO-IO_x (x= 240, 288, 308) films, respectively. In order to achieve a perfect
331 inverse opal structure with a filling fraction close to 26% corresponding to a perfect fcc

332 structure, the filling quantity of the precursor solution, infiltration operation, and heating
 333 rate of the annealing should be appropriate.



334

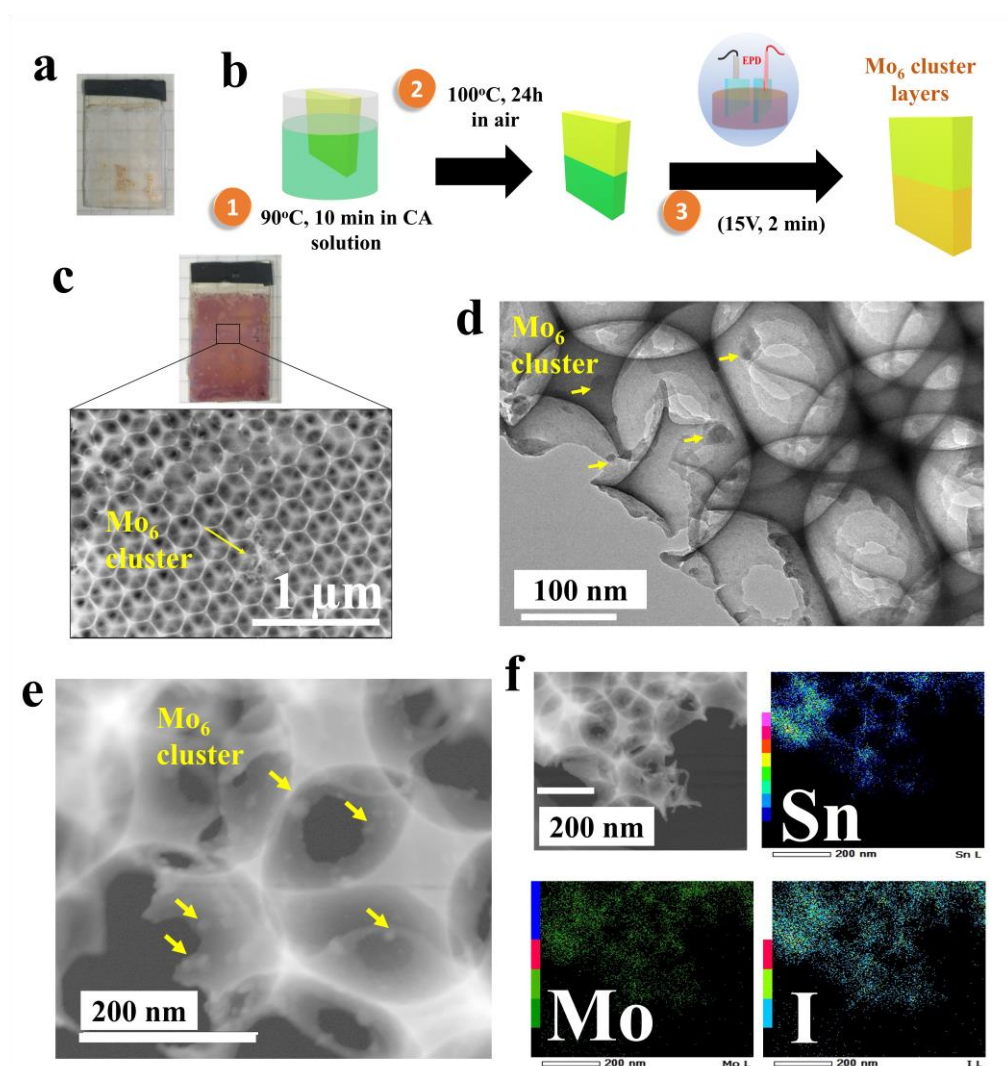
335 Figure 3. (a) X-ray diffraction diagrams of synthesized SnP₂O₇ powder and SnPO IO₂₈₈
 336 film, (b) Schematic illustration of the cubic SnP₂O₇ unit, and the FT-IR spectrum of
 337 SnPO-IO₂₈₈. (c) UV-Vis transmittance spectra and the specular reflectance spectra at the
 338 5 degree incident angle of the SnPO-IO_x films (x= 240, 288, 308) with thermal treatment
 339 at T1 = 550°C and T2 =600°C. (d) Visual photographs and FE-SEM images (left) and
 340 cross-section SEM images of the SnPO-IO_x (x= 240, 288, 308) films. (e) HR-

341 TEM, (h) STEM and schematic image, and (f) STEM-EDX mapping of the SnPO-IO₂₈₈
342 films.

343 **3.2 Characteristics and optical properties of Mo₆ cluster-deposited SnP₂O₇ IO films**

344 The CMI presents the efficiency of the visible light absorbing characteristics, which could
345 be functionalized with an ionic conducting layer of a double hydroxide for tuning the
346 photoconductivity response [12]. The obtained result showed a good photoconductivity
347 response; however, the photosensitivity and photostability needed to be improved. The
348 elimination of the apical iodide ligands of the Mo₆ cluster during the fabrication was also
349 a reason for a reduction of the visible light absorption efficiency. In this study, the
350 anhydrous proton conductor of tin pyrophosphate (SnP₂O₇) was chosen to be combined
351 with the [Mo₆I₁₄]²⁻ cluster unit precursor. As is known, the Cs₂[{Mo₆I₈}I₆^a] solid-state
352 compound is fully dissociated to form the Cs²⁺ cation and [{Mo₆I₈}I₆^a]²⁻ cluster anion in
353 solution. During EPD, hydronium and hydroxide ions, which were generated by the
354 hydrolysis reaction of water in the dispersing medium, will replace some apical ligands
355 to form the [{Mo₆I₈}I_{6-x}^a [OH]_x^a]²⁻ (0 ≤ x ≤ 6) cluster anion in solution which possibly
356 works in the EPD. However, **Fig. 4a** shows a photograph of the SnPO-IO₂₈₈ deposited
357 MI without modification by citric acid with the poor deposition of MI by using the EPD
358 at 15 V for 2 minutes. Surface functionalization of the SnPO-IO_x (x = 240, 288, 308)
359 films was then performed with two treatment steps in a citric acid solution at 90°C for 10
360 minutes and in air at 100°C for 24 hours (**Fig. 4b**). The dried SnP₂O₇ containing
361 negatively-charged oxygen lattice ions can cause an opposite electrostatic interaction with
362 the [{Mo₆I₈}I_{6-x}^a [OH]_x^a]²⁻ (0 ≤ x ≤ 6) cluster anion. For this reason, the citric acid
363 involving three carboxylic acid groups will generate the acidic surface and then becomes
364 a bridge in order to make a second electrostatic interaction with the [{Mo₆I₈}I_{6-x}^a
365 [OH]_x^a]²⁻ (0 ≤ x ≤ 6) cluster anion. These bridges will create hydrogen bonds that are
366 efficient to immobile MI on SnP₂O₇. Moreover, the functionalization by acid groups can
367 improve the interface charge collection efficiency, which is important to carry the electron
368 or ion transport in optoelectronic devices [51]. The deposition of MI on the SnPO-IO₂₈₈
369 film was significantly improved as seen in the photograph with a homogeneous red color
370 which was assigned to the MI nanocluster (**Fig. 4c**). Small cluster aggregates were also

371 observed on the surface of the SnPO-IO_{288ca} film. TEM and STEM were then used to
372 confirm the distribution of MI that exists inside the pores of SnPO-IO_{288ca}-MI (**Fig. 4d**,
373 **e**). STEM-EDX mapping indicated the composition elements of Sn, Mo, and I that
374 confirmed MI nanoparticles with sizes less than 30 nm existing inside the pores (**Fig. 4f**).
375 **Fig. S14** presents the element composition spectrum of Sn, I, and Mo with a poor
376 observation of Cs. As is known, MI is synthesized at high temperatures with a crystal
377 shape. The size of the aggregates of MI was confirmed in the range between 15 and 30
378 nm by the SEM image (**Fig. S15**) which can deposit in the pore size of 267 nm from the
379 SnPO-IO_{288ca}. The concentration and incomplete dissolution of MI in a solvent medium
380 can create small nanoparticles composed of many 2 nm-sized MI clusters with the charge
381 on the surface coming from the MI cluster unit. Only EPD can deposit the $[\text{OH}]^a_x]^{2-}$ ($0 \leq$
382 $x \leq 6$) cluster anion without a counter cation which is an essential part of light harvesting.



383

384 Figure 4. a) Photograph image of SnPO-IO₂₈₈-MI without citric acid modification. b)
 385 Schematic diagram of the fabrication process photos of SnPO-IO_xca and SnPO-IO_xca-MI
 386 films (x = 240, 288, 308). c) Photograph images and FE-SEM images of SnPO-IO₂₈₈ca-
 387 MI with citric acid modification. (d) TEM, (e) STEM, and (f) STEM-EDX mapping
 388 images of SnPO-IO₂₈₈ca-MI.

389

390 **Fig. SI6** summarizes the XPS spectra of SnPO-IO₂₈₈ and SnPO-IO₂₈₈ca-MI. The binding
 391 energy spectra of the Sn3d, P2p, C1s, O1s, Mo 3d, and I 3d regions were measured as
 392 seen in **Table. SI3**. All binding energies were calibrated concerning the C1s peak of the
 393 adventitious carbon at 285 eV. **Table 1** shows the atomic percentages of the elements of

394 SnPO-IO₂₈₈ and SnPO-IO_{288ca-MI}. The atomic ratio of P and Sn is about 1.77. This ratio
 395 is almost unchanged after the EPD (~ 1.73) which indicates the chemical stability of the
 396 SnP₂O₇ inorganic IO film during the hydrolysis reaction. In the SnPO-IO_{288ca-MI} film,
 397 the concentration of carbon atoms increased 2.5 times due to the introduction of citric
 398 acid in comparison to SnPO-IO₂₈₈ without acid treatment. The binding energies assigned
 399 to Sn 3d^{5/2} and Sn 3d^{3/2} of SnPO-IO₂₈₈ were recognized at 487 eV and 495.5 eV,
 400 respectively, with the spin-orbit splitting of the doublet peaks of 8.5±0.1 eV (**Fig. 5a**).
 401 This binding energy confirms the existence of the Sn⁴⁺ cation in SnP₂O₇[34]. The binding
 402 energies assigned to the Sn 3d^{5/2} and Sn 3d^{3/2} regions show a slight change at 486.7 eV
 403 and 495.1 eV for SnPO-IO_{288ca-MI}. The binding energy spectrum of the P 2p region
 404 assigned for P from the PO₄ tetrahedra shows a similar slight shift of the peak from 133.5
 405 eV for SnPO-IO₂₈₈ to 133.3 eV for SnPO-IO_{288ca-MI} (**Fig. 5b**). It can be predicted that
 406 the citric acid can protonate the surface via oxygen in the SnP₂O₇ lattice, as discussed in
 407 detail in the next part. The spectrum of the C1s region shows a strong peak at 284 eV
 408 assigned to the C=C bonding which comes from the decomposed products of polystyrene
 409 existing in SnPO-IO₂₈₈ (**Fig. SI6**). The same result was analyzed for the binding energy
 410 of the O 1s region with a peak at 531 eV from the O-P bonding in both films, and extra
 411 peaks at 533 eV assigned to the O-C and O-H bonds for SnPO-IO_{288ca-MI} in the
 412 convolution spectrum (**Fig. SI6 and Tab. SI5**). The Cs⁺ cation was almost not observed
 413 in the XPS spectrum of SnPO-IO_{288ca-MI} which confirmed the separation of the counter-
 414 cation from the cluster by using EPD. The binding energy spectrum of Mo 3d includes
 415 two specific peaks at 228.7eV (3d^{5/2}) and 231.8 eV (3d^{3/2}) which are assigned to the Mo-
 416 I bonding (**Fig. 5c**). The binding energy peak assigned to Mo-O (235.1) was not observed
 417 which means that the Mo₆ cluster does not oxidize or no valence bonding occurs between
 418 the cluster and other compositions [52]. The deconvolution spectra of I3d are presented
 419 in **Fig. 5d** that shows the peaks assigned to the inner iodine (Iⁱ) at 620.1 eV (3d^{5/2}) and
 420 631.6 eV (3d^{3/2}) and apical iodine (I^a) at 618.4 eV (3d^{5/2}) and 629.9 eV (3d^{3/2}). The
 421 average atomic ratio of Iⁱ and I^a is 8 and 4 which was calculated from the deconvolution
 422 spectra of I3d (**Tab. SI6**). Based on the XPS analysis, the [{Mo₆I₈}I^a₄[OH]^a₂]⁻² cluster
 423 anions were suggested to move to the anode and be neutralized by the hydronium cation
 424 to form [H₃O⁺]₂[{Mo₆I₈}I^a₄[OH]^a₂] or [{Mo₆I₈}I^a₄[H₂O]^a₂].yH₂O cluster compounds as

425 reported earlier [16]. Depending on the total Mo/I atomic ratio of 6/13.6 (theoretical index
 426 is 6:14), the separated iodine anions from the initial cluster were also deposited on an
 427 anode to form the iodide-enriched deposition. A similar conclusion has been revealed
 428 regarding the exchange of two apical ligands and the performance of the
 429 $[\{\text{Mo}_6\text{Br}^{\text{i}}_8\}\text{Br}^{\text{a}}_4[\text{H}_2\text{O}]^{\text{a}_2}]\cdot y\text{H}_2\text{O}$ film enriched Br anion layers which were prepared by
 430 EPD [53]. In summary, the acid modification successfully protonated the SnP_2O_7 lattice
 431 by hydrogen bonding that produced a slight shift in the binding energy of the Sn3d and
 432 P2p regions to the lower range. In addition, the general formula of the cluster in the film
 433 suggested being $[\{\text{Mo}_6\text{I}^{\text{i}}_8\}\text{I}^{\text{a}}_4[\text{H}_2\text{O}]^{\text{a}_2}]\cdot y\text{H}_2\text{O}$, possibly generating an interaction with the
 434 citric acid or SnP_2O_7 through the apical water ligands. This suggestion would support the
 435 electronic conducting transport in the material.

436 Based on the FT-IR spectrum of citric acid (**curve 1**), the absorption peaks of the carbonyl
 437 (C=O) stretching vibration centered at 1759 and 1695 cm^{-1} shift to lower wavenumbers
 438 when citric acid is grafted on the SnP_2O_7 surface as shown in the spectrum of SnPO-
 439 $\text{IO}_{288\text{ca}}$ (**curve 3**) (**Fig. 5e**). The covalent bond between a carboxylic group of the acid
 440 and oxygen on the surface of the SnP_2O_7 lattice can possibly be created by a thermal
 441 treatment, resulting in a shift of the absorption band of the carbonyl (C=O) stretching
 442 vibration. Besides, the wide absorption band in the 1700 and 1000 cm^{-1} range assigned to
 443 the O-H, C-O, C-OH, and C-C vibrations of the citric acid as well as the absorption
 444 bands in the 1300 and 400 cm^{-1} range assigned to the P-O and Sn-O vibration from the
 445 phosphate group (**curve 2**) in SnPO- $\text{IO}_{288\text{ca}}$ were verified (**curve 3**). Once the MI is
 446 immobilized on the IO film, the signal of C=O from the acid in SnPO- $\text{IO}_{288\text{ca}}$ has an
 447 unchanged absorption band. It is suggested that the interaction that occurred between
 448 $[\{\text{Mo}_6\text{I}^{\text{i}}_8\}\text{I}^{\text{a}}_4[\text{H}_2\text{O}]^{\text{a}_2}]$ clusters and citric acid is hydrogen bonds (H-O...H) without
 449 covalent bonding. The chemical structure of MI has not changed after fabrication which
 450 can assure the retainment of the optical absorption characteristic in the visible domain.

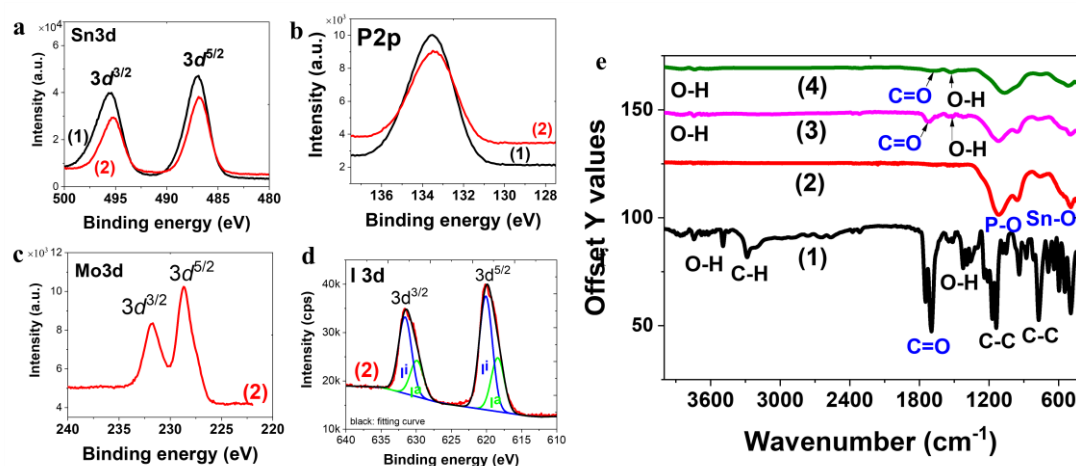
451 **Table 1.** The atomic concentration of the elements of SnPO- IO_{288} and SnPO- $\text{IO}_{288\text{ca}}$ -MI
 452 by the peak analysis of the XPS measurements.

Sn	O	C	P	Cs	Mo	I
----	---	---	---	----	----	---

	% at.						
SnPO-IO₂₈₈	8.32	66.79	4.62	14.75	-	-	- 454
SnPO-IO_{288ca-MI}	8.86	56.91	10.67	14.51	-	2.91	6.56 455
							456

457

458



459

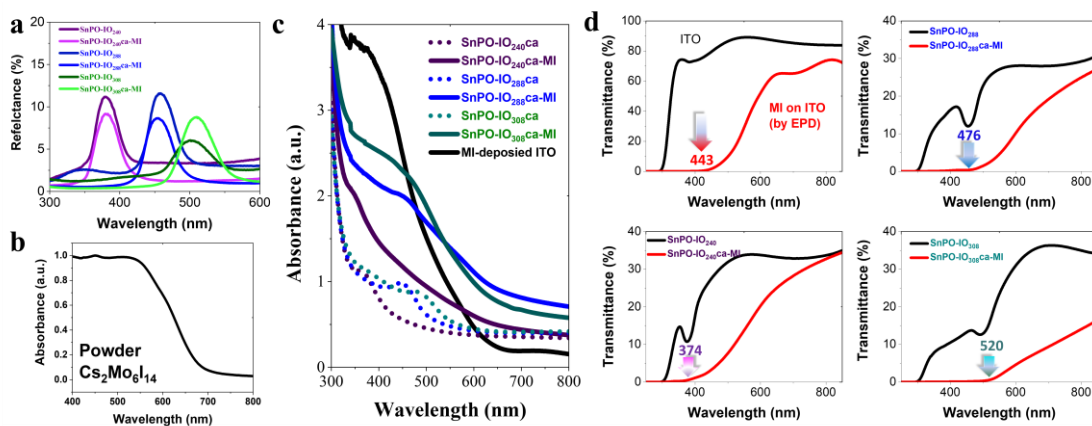
460 Figure 5. XPS binding energy (eV) spectra of SnPO-IO₂₈₈ (1) and SnPO-IO_{288ca-MI} (2)
 461 including (a) Sn3d region, (b) P2p region, (c) Mo3d region, and (d) I3d region. (e) FTIR
 462 spectra of citric acid (1), SnPO-IO₂₈₈ (2), SnPO-IO_{288ca} (3), and SnPO-IO_{288ca-MI} (4).

463 The specular reflectance spectra at the 5-degree incident angle of the SnPO-IO_xca films
 464 (x= 240, 288, 308 nm) from **Fig. SI7** confirm the stability of the ordered porous IO
 465 structure after the citric acid treatment, showing relatively similar stopband peaks. In
 466 order to confirm the different PBGs of the IO films before and after introducing the MI
 467 cluster, the specular reflectance spectra of the IO films were performed (**Fig. 6a**). In **Figs.**
 468 **4d and e**, the MI nanoparticles were anchored on the pore surface, and cluster
 469 concentration was not enough to completely infiltrate the pores or make a thicker SnP₂O₇
 470 wall. For this reason, the stop band peak for the SnPO-IO_xca (x = 240, 288, 308 nm) films
 471 still remains at a similar position to the original band structure after depositing the Mo₆
 472 cluster. In general, the UV-Vis absorption spectrum of MI shows a strong UV-Vis light

473 absorption in the range between 300 and 550 nm and gradually reduces to 670 nm (**Fig.**
474 **6b**). The efficiency of the optical absorption of MI significantly linearly reduces from 400
475 and 600 nm after the MI deposited ITO substrate in comparison to the original powder
476 (**Fig. 6c**). Besides the loss of Cs⁺ cations, the exchange of iodine apical ligands during
477 deposition from $[\{\text{Mo}_6\text{I}_8\}\text{I}_6]^{2-}$ to $[\{\text{Mo}_6\text{I}_8\}\text{I}_4[\text{H}_2\text{O}]_2]_y \cdot \text{H}_2\text{O}$ also caused the reduction
478 of visible light absorption of the Mo₆ cluster. The weak photoluminescence measured for
479 the nanocomposite film shows a difference in comparison to that of the CMI powder (**Fig.**
480 **SI8**). MI appeared to undergo a strong photoluminescence with an emission peak at 700
481 nm after creating a Mo-O covalent bonding with glycine and the layer double hydroxide
482 as reported in a previous study [12]. In this study, the unchanged binding energy of Mo3d
483 proves that the Mo atom of $[\{\text{Mo}_6\text{I}_8\}\text{I}_4[\text{H}_2\text{O}]_2]_y \cdot \text{H}_2\text{O}$ does not create any covalent
484 bonds with other compositions. However, it is well known that hydrolysis of the apical
485 ligands of such a cluster complex leads to a small change in the luminescence spectra
486 [54]. Although the composition modification occurred during fabrication, the CMI
487 powder and MI-deposited ITO film still show the same optical absorption in the range
488 from 400 to 600 nm with a different efficiency, resulting in a similar energy bandgap at
489 1.9 eV which is in agreement with the previous study [16].

490 The absorbance contribution of SnP₂O₇ in the visible light range is zero as seen in the
491 disordered IO powder (dot line) from the transmittance spectrum of **Fig. 3c**. Therefore,
492 the absorbance properties in the visible light of SnPO-IO_xca (x = 240, 288, 308) films
493 will mainly assume the contributions of MI. (**Figs. 6c**). However, the cluster's visible light
494 absorbing range of the Mo₆ cluster in the IO film is expanded to a higher wavelength than
495 the MI-deposited ITO glass. The expansion wavelength range depends on the position of
496 the stopband of the PBGs. The transmittance spectra also confirm the effect of the inverse
497 opal which synergistically improves the light absorption around the original stopband
498 (**Fig. 6d**). The SnPO-IO_xca-MI (x = 240, 288, 308) films show a transmittance of zero at
499 various wavelengths which overlaps with the stop band from the IO structure of SnPO-
500 IO_x even though there is no difference in the EPD parameter, substrate, and MI solution.
501 The size of the MI nanoparticle is an average of 30 nm which is possible to be totally
502 introduced inside 223, 267, and 294 nm-sized pores. The fact that the PBGs in the inverse
503 opal structure are not able to enhance the light absorption because these photons will be

504 reflected in this frequency range. However, a slow photon effect that occurs on the
 505 stopband edges properly enhances the absorption of the material, leading to generating
 506 electron-hole pairs upon irradiation in these wavelength regions [24, 55]. Curti and
 507 colleagues have explained the behavior of the stopband and slow photons at different
 508 positions corresponding to the absorbance region of the material. Depending on their
 509 suggestion, PBGs at 379 nm and the slow photon effect are inactive because their
 510 wavelength is located within the region of the strong absorption of the Mo₆ cluster. In this
 511 case, there is no enhancement of photons for generating electron-hole pairs. On the other
 512 hand, the PBGs at 457 and 502 nm are inactive and their slow photon effects are active.
 513 When the stopband overlaps with the strong absorption region, the reflection will be
 514 avoided and the stopband band edges in the poor absorption region will enhance the light
 515 absorption in this range by slow photon effects. These phenomena are verified by an
 516 enhanced absorption part at higher wavelength ranges in **Fig. 6c**. The enhanced photon in
 517 the absorption region will be scattered inside the pore and absorbed by MI deposited
 518 within the IO structure to generate electron-hole pairs. In summary, the light utilization
 519 capability in the IO structure is improved due to slow photon-induced light absorption
 520 more reasonable than the photonic bandgap-induced light reflection. A few studies also
 521 reported that slow photons of the 3D inverse opal photonic crystals could promote light
 522 absorption of ZnO and TiO₂-Au-CdS for visible photocatalytic activity enhancement [55-
 523 57].

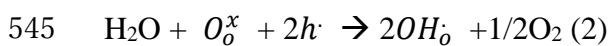


524
 525 **Figure 6.** a) UV-vis absorbance spectra of CMI, b) the specular reflectance spectra at the
 526 5-degree incident angle, c) UV-vis absorbance spectra and d) the transmittance spectra of

527 ITO glass, MI deposited on ITO glass and SnPO-IO_xca, and SnPO-IO_xca-MI (x = 240,
528 288, 308) films.

529 **3.3 Effect of inverse opal structure on the photoconductivity response of Mo₆ cluster-** 530 **functionalized SnP₂O₇ IO film**

531 To understand the electrochemically kinetic information as well as the charge transport
532 on the surface of the SnP₂O₇ bulk and MI cluster units, an illustration of the EIS
533 measurement is presented in **Fig. SI9a**. The experiments were employed for the SnPO-
534 IO₂₈₈, SnPO-IO₂₈₈ca, and SnPO-IO₂₈₈ca-MI films in the humidity and temperature-
535 controlled chamber. The light will directly irradiate the cluster deposited IO film. The
536 interfacial charge transfer resistance (R_{ct}) of the IO films measured at 298 K and 60 %RH
537 was calculated from the fitted value by using a Randles equivalent circuit as depicted in
538 **Fig. SI9b**. The charge transfer resistance (R_{ct}) of SnPO-IO₂₈₈ca was observed to be lower
539 than that of SnPO-IO₂₈₈ corresponding to the smaller semicircle from the Nyquist plots
540 in **Fig. 7a**. In general, SnP₂O₇ nominally does not contain protons in the bulk which is
541 proved by the disappearance of the O-H vibration as seen in the FT-IR spectra in the range
542 between 3500 and 3000 cm⁻¹ (**Fig. 3b**). However, SnP₂O₇ has been reported to exhibit a
543 mixed proton and electron-hole conduction [39,40]. Therefore, the protonation process of
544 SnP₂O₇ during modification in water has been discovered from reaction (2):

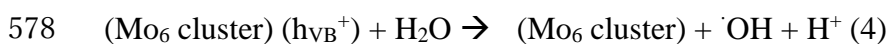
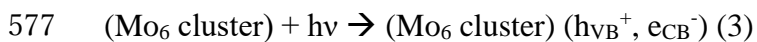


546 Where, O_o^x , $h \cdot$ and OH_o denote a lattice oxide ion, an electron-hole, and a protonated
547 lattice oxide ion, respectively.

548 The appearance of new protons with a high concentration in the SnP₂O₇ bulk was proved
549 by the ¹H MAS NMR spectra reported by Shen et al. [32]. In addition, it was reported that
550 protons migrate via dissociation of the O-H bond (hopping mechanism) [39]. At the
551 humidity of 60% RH, protons coming from the water will interact with lattice oxide ions
552 following reaction (2) to form a protonated lattice oxide ion on the surface of the SnP₂O₇
553 bulk. The introduction of citric acid supports the charge transport on the interface of the
554 conducting IO film by a covalent bond with a protonated lattice oxide ion. It has been
555 claimed that carboxylic acid self-assembled monolayers can reduce the band gap of the

556 initial work function that improves the device performance by aligning the energy levels
 557 in organic optoelectronic devices [51]. Moreover, citric acid contains two another
 558 carboxylic groups for generating hydrogen bonds on the SnP₂O₇ bulk surface which can
 559 accelerate the charge ion transport. As the result, the interfacial charge transport is
 560 improved in SnPO-IO_{288ca}. However, the deposition of $[\{\text{Mo}_6\text{I}_8\}\text{I}_4[\text{H}_2\text{O}]^a_2]_y\text{H}_2\text{O}$
 561 limited the transport of charge on the surface of the SnP₂O₇ bulk by blocking the hydroxyl
 562 groups by the hydrogen bond and made a significant increase in the interfacial charge
 563 transport resistance (R_{ct}) of more than 100 times.

564 However, only the SnPO-IO_{288ca}-MI interestingly shows the AC photoconductivity
 565 response with the photosensitivity of about 0.05 ± 0.01 nS/cm and 0.10 ± 0.01 nS/cm during
 566 the irradiation at fixed wavelengths in the UV range (350 and 370 nm) and visible range
 567 (410, 440, 540 and 580 nm), respectively (**Fig. 7b**). The photosensitivity in the visible
 568 light range (400-600 nm) is more efficient than in ultraviolet light. It can be explained
 569 that the photoconductivity response comes from the $[\{\text{Mo}_6\text{I}_8\}\text{I}_4[\text{H}_2\text{O}]^a_2]_y\text{H}_2\text{O}$ clusters
 570 which strongly absorb in the visible range from 400 to 600 nm and generate photoexcited
 571 clusters containing an electron and a hole as already reported [16]. As is known, the
 572 $[\{\text{Mo}_6\text{X}_8\}\text{X}_6]^{2-}$ (X = halogen) cluster possesses a closed 24 valence electron shell. Some
 573 studies have demonstrated a reversible one-electron oxidation that leads to 23-electron
 574 complexes [58]. On the other hand, during the irradiation of photon energy, the MI cluster
 575 units will generate electron/hole pairs following reaction (3). A hole on the photoexcited
 576 cluster will then react with water to form a proton followed by reaction (4) [12,59].



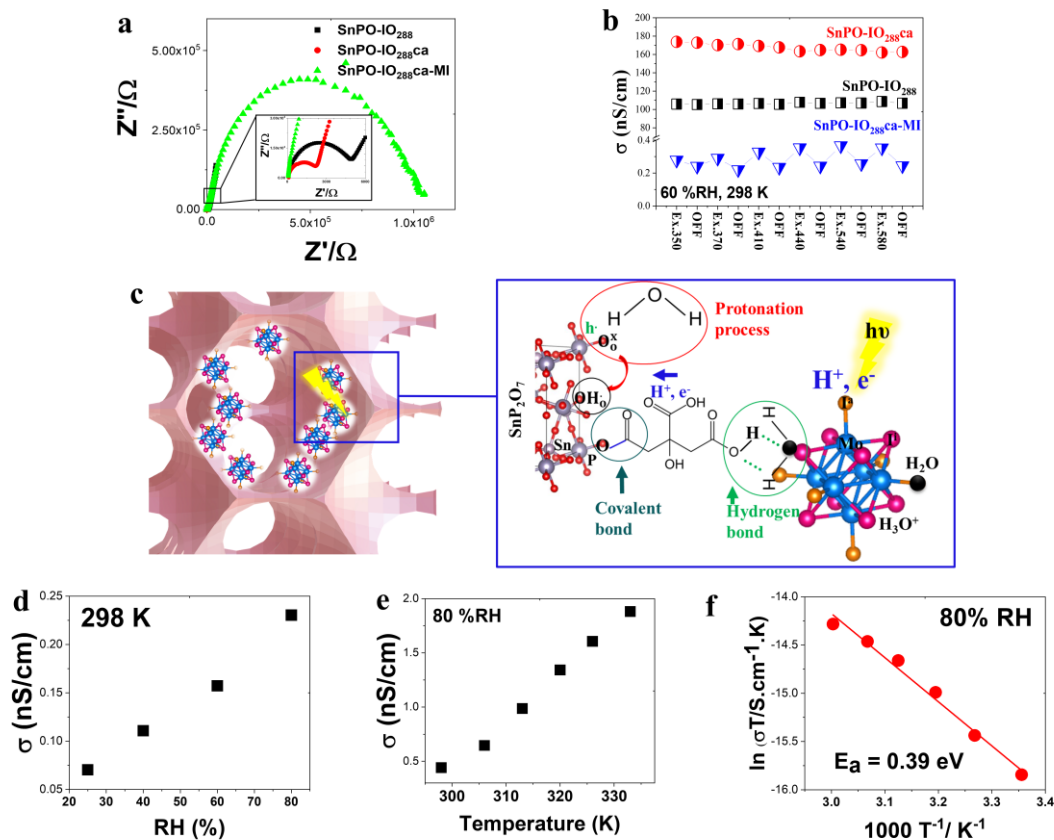
579 A schematic representation of the proton and electron conducting mechanism is
 580 illustrated in **Fig. 7c**. The Mo₆ clusters with apical water are anchored on the surface of
 581 SnP₂O₇ by a hydrogen bond with citric acid which is directly immobilized on SnP₂O₇.
 582 The separated electrons will move from the valence band to the conduction band and are
 583 collected by O-H bonding to move forward to SnP₂O₇ while the generated proton will
 584 continue to move inside the conducting SnP₂O₇ by hydrogen bonds and citric acid bridge.

585 Both electrons and protons, which result in a photoconductivity response, will add to the
586 total conductivity by transporting via the O-H bonds and protonated SnP₂O₇ bulk towards
587 the electrodes. When the illumination was switched off, the electron returned to the Mo₆
588 cluster and OH[•] to form OH⁻ at the surface of SnP₂O₇. The conductivity of the MI film
589 prepared by EPD could not be measured due to the extremely low conductivity coming
590 from MI. As a result, the obtained conductivity of SnPO-IO_{288ca}-MI was essentially
591 contributed by SnP₂O₇ IO and the additive photocurrent comes from the contribution of
592 MI.

593 As is discussed, the protonic conductivity of SnP₂O₇ will be distributed by the water
594 concentration as seen in reaction (2). **Figs. 7d and e**, respectively, present the dependence
595 of the conductivity on the relative humidity (RH) at 298K and the temperature at 80%
596 RH. The deposition of the Mo₆ cluster units does not influence the linear dependence of
597 the protonic and electrical conductivities on the environmental conditions. The activation
598 energy (E_a) was calculated from the relation with the ionic conductivity by Eq. 3:

$$599 \sigma T = A \cdot \exp(-E_a/RT) \quad (3)$$

600 where A is a constant, T is the temperature, R is the gas constant, and E_a is the activation
601 energy. The slope of the fitted Arrhenius plots, wherein the value of the natural logarithm
602 of (σT) is linear versus the temperature (1/K), was used to calculate the activation energy
603 (**Fig. 7f**). The activation energy of SnPO-IO_{288ca}-MI is 0.39 eV that confirms the hopping
604 conduction mechanism [60].



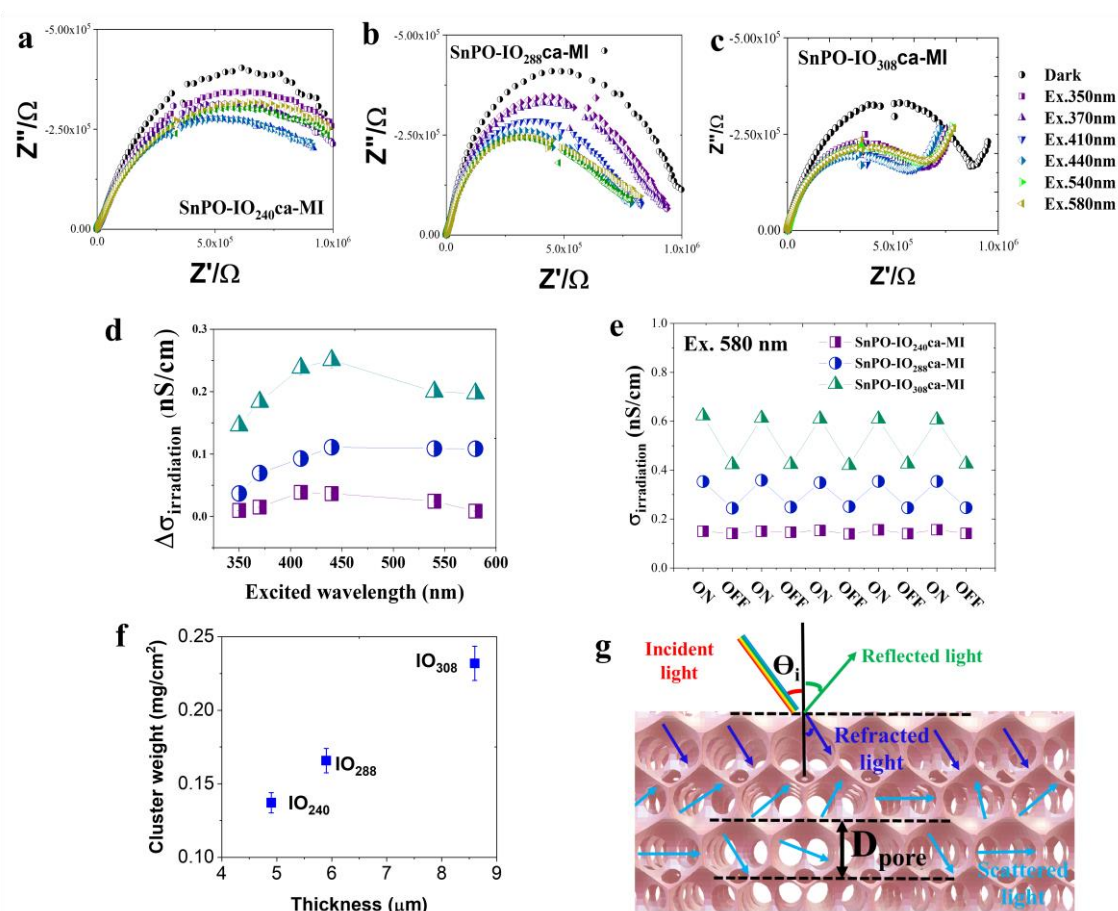
605

606 Figure 7. a) Nyquist plots of SnPO-IO₂₈₈, SnPO-IO_{288ca}, and SnPO-IO_{288ca}-MI at 298K
 607 and 60%RH. (b) The AC photoconductivity response of the films at different irradiation
 608 wavelengths. (c) Schematic representation of the proton and electron conducting
 609 mechanism between SnP₂O₇ and Mo₆ cluster. (d) The dependence of the electrical
 610 conductivity vs. the relative humidity at 298 K, (e) The dependence of the electrical
 611 conductivity vs. the temperatures at 80% RH, and (f) Linear fits of the plots of ln(σT)
 612 versus T⁻¹ of the thin films at different temperatures and humidities.

613 The IO structure with various pore sizes results in a different interfacial charge transport
 614 resistance (R_{ct}) during irradiation of different fixed wavelengths as seen in **Figs. 8 a,b,**
 615 **and c**. The thicknesses of the SnPO-IO_{240ca}-MI, SnPO-IO_{288ca}-MI, and SnPO-IO_{308ca}-MI
 616 films were respectively measured to be 4.9, 5.9, and 8.6 μm (**Fig. S110**). It can be seen
 617 that R_{ct} decreases with a similar tendency for the films irradiated at wavelengths in the
 618 visible domain. SnPO-IO_{308ca}-MI has the lowest R_{ct} which means it produces the best
 619 photocurrent based on **Eq. 1**. The thickness and pore size will contribute to the humidity

620 absorption and the concentration of MI which influences the photocurrent. The increasing
621 photoconductivity of the SnPO-IO_xca-MI (x = 240, 288, 308) films irradiated at the fixed
622 wavelengths of 350, 370, 410, 440, 540, and 580 nm was calculated from **Eq. 1 (Fig. 8d)**.
623 All the films show the best increase in the photoconductivity response at the wavelengths
624 of 410 and 440 nm, then a slight decrease at the wavelength of 580 nm. Several reasons
625 have been considered for the photocurrent result such as i) the transmittance of the ITO
626 glass in the UV range (70%) is lower than that in the visible range (>80%), and ii) the
627 photon energy in the UV range is partially adsorbed by SnP₂O₇ (**Fig. 3c**). The
628 reproducibility and photosensitization of the photoconductivity are important points for
629 use in optical-related devices. The AC photocurrents of the films irradiated at the fixed
630 wavelength of 580 nm were measured for 5 cycles with every measurement performed
631 for 3 minutes without stopping (**Figs. 8e**). The photosensitization of SnPO-IO₂₄₀ca-MI,
632 SnPO-IO₂₈₈ca-MI, and SnPO-IO₃₀₈ca-MI was, respectively, 0.034, 0.11, and 0.19 nS/cm
633 irradiated at the wavelength of 580 nm. All the films obtained a good reproducibility of
634 the photocurrent after 5 cycles of the EIS measurement. As seen in Fig. 8f, the deposited
635 Mo₆ concentration is proportional to the thickness of the films which are determined by
636 0.14, 0.17, and 0.23 mg/cm² corresponding to the thickness value at 4.9, 5.9, and 8.6 μm,
637 respectively, for SnPO-IO₂₄₀, SnPO-IO₂₈₈, and SnPO-IO₃₀₈. For the same EPD
638 parameters, the bigger the PS bead size, the larger the pore size, and the thicker the IO
639 film. During EPD, the charged PS particles smoothly move toward the IO electrode within
640 a greater pore volume, resulting in more Mo₆ clusters in thicker IO film. Moreover, the
641 incidence light will be reflected at the stopband while the absorption light will be
642 enhanced at the stopband edges by an impact of slow photons which occur for the poor
643 absorption region. As is discussed in **Fig. 6**, only the films which show the PBGs at 457
644 and 502 nm can activate a low photon effect. The enhanced absorbance light will be
645 mostly scattered within the pore and adsorbed by the Mo₆ cluster (**Fig. 8g**). Moreover,
646 the scattering light will be proportionally enhanced with the increase in the macropore
647 size. As the result, the IO film containing PBG at 502 nm that its stopband edge overlaps
648 with to excitation wavelength at 580 nm can show the highest ability to generate electron-
649 hole pairs for increasing the photocurrent upon illumination at this wavelength. In
650 summary, the baseline current will be affected by the thickness of SnP₂O₇, while the

651 photocurrent depends on the MI concentration controlled by the thickness, active porous
 652 areas, and the slow photon effect in the stopband edges.

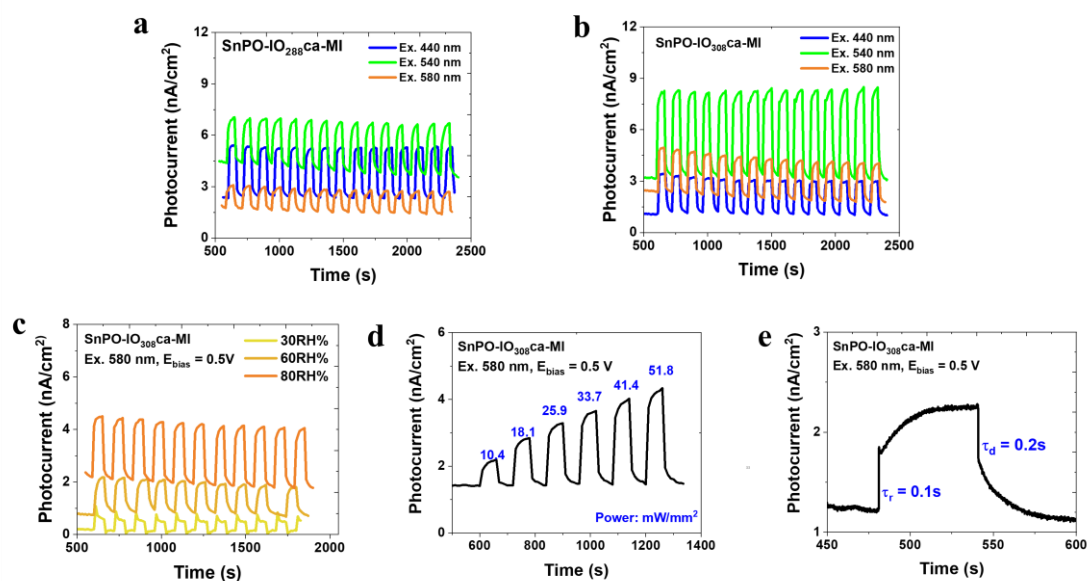


653

654 Figure 8. Nyquist plots of (a) SnPO-IO₂₄₀-ca-MI, (b) SnPO-IO₂₈₈-ca-MI, and (c) SnPO-
 655 IO₃₀₈-ca-MI films. d) The AC photoconductivity response of SnPO-IO_x-ca-MI (x = 240,
 656 288, 308) films at different excitation wavelengths at 297K and RH 60%. e) Repeatability
 657 of photoconductivity response of SnPO-IO_x-ca-MI (x = 240, 288, 308) films irradiated at
 658 the fixed wavelength of 580 nm. f) Schematic illustration of the absorption light scattered
 659 by the IO structure.

660 The reproducible on/off switching curves of the DC photocurrent at the bias voltage of
 661 the 0.5 V of SnPO-IO_x-ca-MI (x = 288, and 308) films are presented in **Figs. 9a and b**,
 662 respectively. The measurement of SnPO-IO₂₄₀-ca-MI was skipped in this experiment
 663 because the slow photon effect does not occur at the stopband edge of PBG. It is noted
 664 that the DC photoconductivity responses depend on light illumination at the wavelengths

665 of 440, 540, and 580 nm at the relative humidity (RH) of 80% and 298 K. The
666 photocurrents from various excitation wavelengths have different baselines due to
667 currents that are not stable after a continual and long measurement time. The excitation
668 light at wavelengths, which overlapped with the stopband edges of PBG results in a
669 leading light absorption in these wavelengths. This would explain the highest observed
670 photocurrents; the slow photon effect occurs around PBG at 453 nm of the SnPO-IO₂₈₈ca-
671 MI which is near the irradiation light of 440 nm (Fig. 9a), whereas SnPO-IO₃₀₈ca-MI
672 shows a slow photon somewhere closer to 540 nm (Fig. 9b). Both films with different
673 pore sizes result in a stable photocurrent reproducibility after 15 cycles. Reproducible
674 on/off switching curves at the 580 nm illumination of the nanocomposite films measured
675 at different humidities and 298 K are shown in **Fig. 9c** and **Fig. SI11**. The photocurrent
676 response is proportional to the relative humidity which agreed with **Fig. 7d** following the
677 hopping conduction mechanism. At the temperature of 298K and RHs of 30%, 60%, and
678 80%, the photosensitive of SnPO-IO₃₀₈ca-MI was recognized to be about 0.11, 1.29, and
679 2.41 nA/cm² during the irradiation of the fixed wavelengths at 580 nm, respectively.
680 Humidity plays an essential role to provide a water carrier that accelerates the movement
681 of ions and electrons. In addition, the photocurrent also shows a linear dependence on the
682 illumination power (**Fig. 9d**). The rising and decaying photocurrent responses (τ) were
683 measured at 0.1 and 0.2 s, indicating a rapid photoresponse characteristic (**Fig. 9e**). The
684 reproductivity of the photoconductivity was also obtained in a short time that improved
685 in comparison to the layer double hydroxides functionalized by MI clusters in a previous
686 report [12]. This result is more interesting for the application of environmental sensors or
687 visible photodetectors.



688

689 Figure 9. Reproducible on/off switching curves of DC photocurrent at a bias voltage of
 690 0.5 V of a) the SnPO-IO₂₈₈ca-MI film and b) SnPO-IO₃₀₈ca-MI film during the
 691 illumination by different light wavelengths measured at RH of 80 % and 298 K versus
 692 the time, and c) SnPO-IO₃₀₈ca-MI film during the illumination by the wavelengths of 580
 693 nm measured at different humidities and 298 K versus the time. d) The DC photocurrent
 694 of the SnPO-IO₃₀₈ca-MI film during the illumination by the wavelengths of 580 nm
 695 measured at the RH of 80%, 298 K, and different powers versus irradiation power. e)
 696 Enlarged rising and decaying edges of the photocurrent response of the SnPO-IO₃₀₈ca-
 697 MI film (298 K, 80 %RH) during the illumination of power at the 51.8 mW/mm².

698 A good photosensitization and reproducibility depend on the interfacial charge transport
 699 which is contributed by the protonic and electrical conductivities coming from the Mo₆
 700 cluster, SnP₂O₇, and an acid bridge between them. The proton conductivity of three
 701 molybdenum cluster-based materials as building blocks, (H)₄[Mo₆Br₆S₂(OH)₆]-12H₂O
 702 and (H)₂[Mo₆X₈(OH)₆]-12H₂O (X = Cl, Br), was reported for the first time with the good
 703 conductivity of $1.4 \times 10^{-4} \text{ S} \cdot \text{cm}^{-1}$ under wet conditions for (H)₂[Mo₆Cl₈(OH)₆]-12H₂O
 704 (X = Cl, Br) [61]. It is possibly claimed that concerted proton transfers through the
 705 hydrogen-bond network and vehicular (or diffusion) transport probably occur within the
 706 materials. During the irradiation, it was proved that the excited electron enhanced the
 707 charge on the surface of the Mo₆ cluster and was easily transported in the network [15].

708 The covalent and hydrogen bonds generated between the Mo₆ cluster with graphene
709 oxide, silica oxide, hexagonal boron nitride, and layered double hydroxide have been
710 reported that achieved an excellent photooxidation for a catalyst and photocurrent for
711 optoelectronic materials [12, 62-64]. Hence, the strategy for the improvement of this
712 material in the future is to find a new approach for improving the photon and electrical
713 photoconductivity of the SnP₂O₇ IO films by doping some different metals, such as In,
714 Al, and Mg elements, and creating covalent bonding with the Mo₆ cluster.

715 **4. CONCLUSIONS**

716 For the first time, the 3D SnP₂O₇ conducting inverse opals with different pore size
717 intergrated Mo₆ clusters were successfully fabricated by electrophoretic deposition and
718 thermal treatment. The acid surface modification of the SnP₂O₇ IO films results in an
719 improvement of the deposited concentration of the Mo₆ cluster. The covalent bonding
720 was recognized between the citric acid and SnP₂O₇ IO films by FTIR and XPS. The
721 [$\{\text{Mo}_6\text{I}_8\}\text{I}_4[\text{H}_2\text{O}]_2\cdot y\text{H}_2\text{O}$] cluster compound still retained the octahedral structure with
722 a poor existence of Cs⁺ counter-cations and exchanging of the two apical iodide ligands
723 compared to the Cs₂[$\{\text{Mo}_6\text{I}_8\}\text{I}_6$] precursor. The SnP₂O₇ IO films exhibited PBG at 379,
724 457, and 502 nm, and their stopband edges activated the slow photon effect to enhance
725 the optical adsorbing property of the Mo₆ cluster. Interestingly, the photocurrent response
726 during the irradiation of visible light with a high photosensitivity efficiency comes from
727 the Mo₆ cluster-functionalized SnP₂O₇ IO films. The protons and electrons conducting
728 mechanism of the SnP₂O₇ IO films combines the proton and electrical conductivities via
729 hydrogen bonding (a vehicular mechanism). The reproducibility and photostability of the
730 nanocomposite were confirmed by both EIS measurement and DC measurement. This
731 study will contribute to the achievement of the nanocomposite family that can show an
732 efficient photoconductivity response in the visible domain, an important characteristic of
733 materials for applications of water splitting, photodetectors, and photoelectrodes for dye-
734 sensitized solar cells.

735 **AUTHOR CONTRIBUTIONS**

736 Thi Kim Ngan Nguyen conceived and designed the experiments; performed the
737 experiments, analyzed and interpreted the data, and drafted the article. Fabien Grasset and
738 Stephane Cordier analyzed and interpreted the data; and drafted the article. Noee Dumait
739 performed the experiments. Satoshi Ishii, Hiroshi Fudouzi, and Tetsuo Uchikoshi
740 critically revised to improve the intellectual content.

741 **ACKNOWLEDGMENTS**

742 These studies were carried out as part of the France-Japan International Collaboration
743 Framework (IRL3629 LINK) with the partial support of Dr. David Berthebaud as
744 director. T.K.N. Nguyen thanks to the International Center for Young Scientists (ICYS-
745 Sengen) and NIMS for the continued financial support. I would like to thank Prof. Naoto
746 Shirahata for his useful advice and Dr. Cédric Bourgès for his XRD analysis.

747 **APPENDIX A. SUPPLEMENTARY MATERIAL**

748 Supplementary data to this article can be found online at

749 **REFERENCES**

- 750 [1] A. Chetia, J. Bera, A. Betal, S. A. Sahu, brief review on photodetector performance
751 based on zero-dimensional and two dimensional materials and their hybrid structures.
752 *Materials Today Communications*, 30 (2022) 103224.
753 <https://doi.org/10.1016/j.mtcomm.2022.103224>.
- 754 [2] B. Ezhilmaran, A. Patra, S. Benny, M. R. Sreelakshmi, V. V. S. Akshay, S.
755 Venkataprasad Bhat, C.S. Rout, Recent developments in the photodetector applications
756 of Schottky diodes based on 2D materials. *J. Mater. Chem. C*, 9 (2021) 6122-6150.
757 <https://doi.org/10.1039/D1TC00949D>
- 758 [3] F. S. Liang, S. J. Wang, S. P. Li, L. B. Luo, Near-Infrared-Light Photodetectors Based
759 on One-Dimensional Inorganic Semiconductor Nanostructures. *Advanced Optical*
760 *Materials*, 5 (2017) 1700081. <https://doi.org/10.1002/adom.201700081>
- 761 [4] M. Manikandan, D. Nirmal, J. Ajayan, B. Mohankumar, P. Prajoon, L. Arivazhagan,
762 A review of blue light emitting diodes for future solid state lighting and visible light

763 communication applications. *Superlattices and Microstructures*. 136 (2019) 106294.
764 <https://doi.org/10.1016/j.spmi.2019.106294>

765 [5] A. Minotto, P. A. Haigh, L. G. Łukasiewicz, E. Lunedei, D. T. Gryko, I. Darwazeh,
766 F. Cacialli, Visible light communication with efficient far-red/near-infrared polymer
767 light-emitting diodes. *Light Sci. Appl.*, 9 (2020) 70-81. [https://doi.org/10.1038/s41377-](https://doi.org/10.1038/s41377-020-0314-z)
768 [020-0314-z](https://doi.org/10.1038/s41377-020-0314-z)

769 [6] K. Kirakci, S. Cordier, C. Perrin, Synthesis and Characterization of Cs₂Mo₆X₁₄ (X =
770 Br or I) Hexamolybdenum Cluster Halides: Efficient Mo₆ Cluster Precursors for Solution
771 Chemistry Syntheses. *Z. Anorg. Allg. Chem.*, 63 (2005) 411-416.
772 <https://doi.org/10.1002/zaac.200400281>

773 [7] B. Dierre, K. Costuas, N. Dumait, S. Paofai, M. Amela-Cortes, Y. Molard, F. Grasset,
774 Y. Cho, K. Takahashi, N. Ohashi, T. Uchikoshi, S. Cordier. Mo₆ cluster-based
775 compounds for energy conversion applications: comparative study of photoluminescence
776 and cathodoluminescence. *Sci. Technol. Adv. Mater.*, 181 (2017) 458-466.
777 DOI: 10.1080/14686996.2017.1338496

778 [8] M. Prévôt, M. Amela-Cortes, S.K. Manna, R. Lefort, S. Cordier, H. Folliot, L. Dupont,
779 Y. Molard, Design and Integration in Electro-Optic Devices of Highly Efficient and
780 Robust Red-NIR Phosphorescent Nematic Hybrid Liquid Crystals Containing
781 [Mo₆I₈(OCOCnF_{2n+1})₆]²⁻ (n = 1, 2, 3) Nanoclusters. *Adv. Funct. Mater.*, 25 (2015)
782 4966–4975. <https://doi.org/10.1002/adfm.201501876>

783 [9] P. S. Kuttipillai, Y. Zhao, C. J. Traverse, R. J. Staples, B. G. Levine, R. R. Lunt,
784 Phosphorescent Nanocluster Light-Emitting Diodes. *Adv. Mater.*, 18 (2016) 320–326.
785 <https://doi.org/10.1002/adma.201504548>

786 [10] E. F. Molina, N. A. Martins de Jesus, S. Paofai, P. Hammer, M. Amela-Cortes, M.
787 Robin, S. Cordier, Y. Molard, When a Red–NIR-Emissive Cs₂[Mo₆Br₁₄] Interacts with
788 an Active Diureasil–PEO Matrix: Design of Tunable and White-Light-Emitting Hybrid
789 Material. *Chem. Eur. J.*, 25 (2019) 15248 – 15251.
790 <https://doi.org/10.1002/chem.201903892>

791 [11] T. K. N. Nguyen, A. Renaud, M. Wilmet, N. Dumait, S. Paofai, B. Dierre, W. Chen,
792 N. Ohashi, S. Cordier, F. Grasset, T. Uchikoshi, New ultraviolet and near-infrared
793 blocking filters for energy saving applications: fabrication of tantalum metal atom cluster-

794 based nanocomposite thin films by electrophoretic deposition. *J. Mater. Chem. C*, 5
795 (2017)10477-10484. <https://doi.org/10.1039/C7TC02454A>

796 [12] T. K. N. Nguyen, N. Dumait, F. Grasset, S. Cordier, D. Berthebaud, Y. Matsui,
797 N. Ohashi, T. Uchikoshi, Zn–Al Layered Double Hydroxide Film Functionalized by a
798 Luminescent Octahedral Molybdenum Cluster: Ultraviolet–Visible Photoconductivity
799 Response. *ACS Applied Materials & Interfaces*, 12 (2020) 40495-40509. [https://doi.org/](https://doi.org/10.1021/acsami.0c10487ff)
800 [10.1021/acsami.0c10487ff](https://doi.org/10.1021/acsami.0c10487ff). [ffhal-02930344](https://doi.org/10.1021/acsami.0c10487ff)

801 [13] A. Renaud, T.K.N. Nguyen, F. Grasset, M. Raissi, V. Guillon, F. Delabrouille, N.
802 Dumait, P. Y. Jouan, L. Cario, S. Jobic, Y. Pellegrin, F. Odobel, S. Cordier, T. Uchikoshi,
803 Preparation by electrophoretic deposition of molybdenum iodide cluster-based functional
804 nanostructured photoelectrodes for solar cells. *Electrochimica Acta*, 17 (2019) 37-745.
805 <https://doi.org/10.1016/j.electacta.2019.05.154>

806 [14] M. Feliz, P. Atienzar, M. Amela-Cortés, N. Dumait, P. Lemoine, Y. Molard,
807 S. Cordier, Supramolecular Anchoring of Octahedral Molybdenum Clusters onto
808 Graphene and Their Synergies in Photocatalytic Water Reduction. *Inorganic Chemistry*,
809 58 (2019)15443-15454. <https://doi.org/10.1021/acs.inorgchem.9b02529>

810 [15] K. Harada, T. K. N. Nguyen, F. Grasset, C. Comby-Zerbino, L. MacAleese, F.
811 Chirot, P. Dugourd, N. Dumait, S. Cordier, N. Ohashi, M. Matsuda, T. Uchikoshi, Light-
812 dependent ionic-electronic conduction in an amorphous octahedral molybdenum cluster
813 thin film. *NPG Asia Mater.*, 14 (2022) 21. <https://doi.org/10.1038/s41427-022-00366-8>

814 [16] A. Renaud, P. V. Jouan, N. Dumait, S. Ababou-Girard, N. Barreau, T. Uchikoshi, F.
815 Grasset, S. Jobic, S. Cordier, Evidence of the Ambipolar Behavior of Mo₆ Cluster Iodides
816 in All-Inorganic Solar Cells: A New Example of Nanoarchitectonic Concept. *ACS*
817 *Applied Materials & Interfaces*, 14 (2022) 347-1354.
818 <https://doi.org/10.1021/acsami.1c17845>

819 [17] S. Khlifi, J. Bignon, M. Amela-Cortes, N. Dumait, G. Loas, S. Cordier, Y. Molard,
820 Switchable Two-Dimensional Waveguiding Abilities of Luminescent Hybrid
821 Nanocomposites for Active Solar Concentrators. *ACS Applied Materials & Interfaces*, 12
822 (2020)14400-14407. <https://doi.org/10.1021/acsami.9b23055>

823 [18] M. Shkir, M. T. Khan, I. M. Ashraf, A. Almohammed, E. Dieguez, S. AlFaify, High-
824 performance visible light photodetectors based on inorganic CZT and InCZT single

825 crystals. *Scientific Reports*, 9 (2019) 12436. [https://doi.org/10.1038/s41598-019-48621-](https://doi.org/10.1038/s41598-019-48621-3)
826 3

827 [19] P. H. Chung, C. T. Kuo, T. H. Wang, Y. Y. Lu, C. I. Liu, T.R. Yew. A Sensitive
828 Visible Light Photodetector Using Cobalt-Doped Zinc Ferrite Oxide Thin Films, *ACS*
829 *Appl. Mater. Interfaces*, 13 (2021) 6411–6420. <https://doi.org/10.1021/acsami.0c20487>

830 [20] S. Yanikgonul, V. Leong, J. R. Ong, T. Hu, S. Y. Siew, C. E. Png. L. Krivitsky,
831 Integrated avalanche photodetectors for visible light. *Nature Communications*, 12
832 (2021) 1834. <https://doi.org/10.1038/s41467-021-22046-x>

833 [21] T. Ji, Q. Liu, R. Zou, Y. Zhang, L. Wang, L. Sang, M. Liao, J. Hu, Enhanced UV-
834 visible light photodetectors with a TiO₂/Si heterojunction using band engineering. *J.*
835 *Mater. Chem. C*, 5 (2017) 12848–12856. <https://doi.org/10.1039/C7TC04811D>

836 [22] E. Armstrong, C. O'Dwyer, Artificial opal photonic crystals and inverse opal
837 structures – fundamentals and applications from optics to energy storage. *J. Mater. Chem.*
838 *C*, 3 (2015) 109–1143. DOI <https://doi.org/10.1039/C5TC01083G>

839 [23] C. I. Aguirre, E. Reguera, and A. Stein, Tunable Colors in Opals and Inverse Opal
840 Photonic Crystals, *Adv. Funct. Mater.*, 20 (2010) 2565–2578
841 <https://doi.org/10.1002/adfm.201000143>

842 [24] M. Curti, J. Schneider, D. W. Bahnemann, C. B. Mendive, Inverse Opal Photonic
843 Crystals as a Strategy to Improve Photocatalysis: Underexplored Questions, *J. Phys.*
844 *Chem. Lett.*, 6 (2015) 3903–3910, <https://doi.org/10.1021/acs.jpcllett.5b01353>

845 [25] Y. Gun, G. Y. Song, V. H. V. Quy, J. Heo, H. Lee, K.S. Ahn, S. H. Kang, Joint
846 Effects of Photoactive TiO₂ and Fluoride-Doping on SnO₂ Inverse Opal
847 Nanoarchitecture for Solar Water Splitting, *ACS Appl. Mater. Interfaces*, 7 (2015)
848 20292–20303 <https://doi.org/10.1021/acsami.5b05914>

849 [26] F. Temerov, K. Pham, P. Juuti, J. M. Makela, E. V. Grachova, S. Kumar, S. Eslava,
850 J. J. Saarinen, Silver-Decorated TiO₂ Inverse Opal Structure for Visible Light- Induced
851 Photocatalytic Degradation of Organic Pollutants and Hydrogen Evolution, *ACS Appl.*
852 *Mater. Interfaces*, 12 (2020) 41200–41210 <https://doi.org/10.1021/acsami.0c08624>

853 [27] L. Zhang, E. Reisner, J. J. Baumberg, Al-doped ZnO inverse opal networks as
854 efficient electron collectors in BiVO₄ photoanodes for solar water oxidation, *Energy*
855 *Environ. Sci.*, 7 (2014)1402–1408 <https://doi.org/10.1039/C3EE44031A>

856 [28] J. Wang, Y. Yuan, H. Zhu, T. Cai, Y. Fang, O. Chen, Three-dimensional
857 macroporous photonic crystal enhanced photon collection for quantum dot-based
858 luminescent solar concentrator, *Nano Energy*, 67 (2020) 104217.
859 <https://doi.org/10.1016/j.nanoen.2019.104217>

860 [29] D.Gaillot, T. Yamashita, C. J. Summers, Photonic band gaps in highly conformal
861 inverse-opal based photonic crystals. *Physical Review B*, 2 (2005) 205109.
862 <https://doi.org/10.1103/PhysRevB.72.205109>

863 [30] Z. Cai, Y. Yan, L. Liu, S. Lin, H.Hu, Controllable fabrication of metallic photonic
864 crystals for ultra-sensitive SERS and photodetectors. *RSC Adv.*, 7 (2017) 5851–55858.
865 <https://doi.org/10.1039/C7RA11721C>

866 [31] K. Xie, M. Guo, H.Huang, Photonic crystals for sensitized solar cells: fabrication,
867 properties, and applications. *J. Mater. Chem. C*, 3 (2015) 10665-10686.
868 <https://doi.org/10.1039/C5TC02121A>.

869 [32] Y. Shen, M. Nishida, W. Kanematsu, T. Hibino, Synthesis and characterization of
870 dense SnP₂O₇–SnO₂ composite ceramics as intermediate-temperature proton conductors.
871 *Journal of Materials Chemistry*, 21 (2011) 663–670.
872 <https://doi.org/10.1039/C0JM02596H>

873

874 [33] K. S. Lee, S. Maurya, Y. S. Kim, C. R. Kreller, M. S. Wilson, D. Larsen, S. E.
875 Elangovan, R.Mukundan, Intermediate temperature fuel cells via an ion-pair coordinated
876 polymer electrolyte. *Energy Environ. Sci.*, 1 (2018) 979-987.
877 <https://doi.org/10.1039/C7EE03595K>

878 [34] K. P. Ramaiyan, S.Herrera, M. J. Workman, T. A. Semelsberger, V. Atanasov, J.
879 Kerres, S. Maurya, Y. S. Kim, C. R. Kreller, R.Mukundan, Role of phosphate source in
880 improving the proton conductivity of tin pyrophosphate and its electrolytes. *J. Mater.*
881 *Chem. A*, 2020, 8, 16345-16354. <https://doi.org/10.1039/D0TA04327C>

882 [35] J. Pan, S. Chen, D. Zhang, S.Xu, Y. Sun, F. Tian, P. Gao, J. Yang, SnP₂O₇ Covered
883 Carbon Nanosheets as a Long-Life and High-Rate Anode Material for Sodium-Ion

884 Batteries. *Advanced Functional Materials*, 2018, 28, 1804672.
885 <https://doi.org/10.1002/adfm.201804672>

886 [36] I. Bezzaa, V. Trouillet, A. Fiedler, M. Bruns, S. Indris, H. Ehrenberg, I. Saadoune,
887 Understanding the lithiation/delithiation process in SnP₂O₇ anode material for lithium-
888 ion batteries. *Electrochimica Acta*, 252 (2017) 446–452.
889 <https://doi.org/10.1016/j.electacta.2017.09.023>

890 [37] P.Lv, T. Ito, A. Oogushi, K. Nakashima, M. Nagao, T. A Hibino, self-regenerable
891 soot sensor with a proton-conductive thin electrolyte and a nanostructured platinum
892 sensing electrode. *Sci. Rep.*, 6 (2016) 37463. <https://doi.org/10.1038/srep37463>

893 [38] J. Zhong, C. Li, W. Zhao, S. You, J. Brgoch, Accessing High-Power Near-Infrared
894 Spectroscopy Using Cr³⁺-Substituted Metal Phosphate Phosphors. *Chemistry of*
895 *Materials*, 34 (2022) 337-344. <https://doi.org/10.1021/acs.chemmater.1c03671>

896 [39] M. Nagao, T. Kamiya, P. Heo, A. Tomit, T. Hibino, M. Sanoa, Proton Conduction in
897 In³⁺ Doped SnP₂O₇ at Intermediate Temperatures. *Journal of The Electrochemical*
898 *Society*, 53 (2006) 604-1609. <https://doi.org/10.1149/1.2210669>

899 [40] H. Wang, J. Xiao, Z. Zhou, F. Zhang, H. Zhang, G. Ma, Ionic conduction in undoped
900 SnP₂O₇ at intermediate temperatures. *Solid State Ionics*, 81 (2010), 1521–1524.
901 <https://doi.org/10.1016/j.ssi.2010.08.029>

902 [41] J. F. Dechezelles, T. Aubert, F. Grasset, S. Cordier, C. Barthou, C. Schwob, A.
903 Maitre, R. A. L. Vallee, H. Cramaild, S. Ravaine, Fine tuning of emission through the
904 engineering of colloidal crystals *Phys. Chem. Chem. Phys.*, 12 (2010), 11993–11999
905 <https://doi.org/10.1039/C0CP00129E>

906 [42] A. Renaud, F. Grasset, B. Dierre, T. Uchikoshi, N. Ohashi, T. Takei, A. Planchat, L.
907 Cario, S. Jobic, B. Odobel, S. Cordier, Inorganic Molybdenum Clusters as Light-
908 Harvester in All Inorganic Solar Cells: A Proof of Concept, *Chemistry Select*, 1 (2016),
909 2284-2289 <https://doi.org/10.1002/slct.201600508>

910 [43] S. Furumi, H. Fudouzi, T. Sawadaa, Dynamic photoswitching of micropatterned
911 lasing in colloidal crystals by the photochromic reaction. *J. Mater. Chem.*, 2 (2012),
912 21519–21528. <https://doi.org/10.1039/C2JM34747D>

913 [44] T. Roisnel, J. Rodriguez-Carvajal, WinPLOTR: a Windows tool for powder
914 diffraction patterns analysis, *Materials Science Forum*, Ed. R. Delhez and E.J.
915 Mittenmeijer, 378-381 (2001) 118-123.

916 [45] J. Rodríguez-Carvajal, Recent Developments of the Program FULLPROF,
917 Newsletter in Commission on Powder Diffraction (IUCr), 2001, 26, 12.

918 [46] K. Katagiri, Y. Tanaka, K. Uemura, K. Inumaru, T. Seki, Y. Takeoka, Structural color
919 coating films composed of an amorphous array of colloidal particles via electrophoretic
920 deposition. *Npg Asia Materials*, 9 (2017) 355-362. <https://doi.org/10.1038/am.2017.13>

921 [47] F. Fayon, I. J. King, R. K. Harris, R. K. B. Gover, J. S. O. Evans, D. Massiot,
922 Characterization of the Room-Temperature Structure of SnP₂O₇ by 31P Through-Space
923 and Through-Bond NMR Correlation Spectroscopy. *Chem. Mater.*, 5 (2003) 2234-2239.
924 <https://doi.org/10.1021/cm031009d>

925 [48] L. Kőrösi, S. Papp, V. Meynen, P. Cool, E. F. Vansant, I. Dékány, Preparation and
926 characterization of SnO₂ nanoparticles of enhanced thermal stability: The effect of
927 phosphoric acid treatment on SnO₂·nH₂O. *Physicochemical and Engineering Aspects*,
928 268 (2005) 147-154. <https://doi.org/10.1016/j.colsurfa.2005.05.074>

929 [49] H. Wang, J. Xiao, Z. Zhou, F. Zhang, H. Zhang, G. Ma, Ionic conduction in undoped SnP₂O₇
930 at intermediate temperatures. *Solid State Ionics*, 2010, 81, 1521–1524.

931 [50] A. Richel, N. P. Johnson and D. W. McComb Observation of Bragg reflection in
932 photonic crystals synthesized from air spheres in a titania matrix *Appl. Phys. Lett.* 76,
933 1816 (2000); <https://doi.org/10.1063/1.126175>

934 [51] N. Kramer, S. Sarkar, L. Kronik, N. Ashkenasy, Systematic modification of the
935 indium tin oxide work function via side-chain modulation of an amino-acid
936 functionalization layer. *Phys. Chem. Chem. Phys.*, 21 (2019) 21875-21881.
937 <https://doi.org/10.1039/C9CP04079J>

938 [52] T. K. N. Nguyen, Y. Matsuia, N. Shirahata, N. Dumait, S. Cordier, F. Grasset, N.
939 Ohashi, T. Uchikoshi, Zn-Al layered double hydroxide-based nanocomposite
940 functionalized with an octahedral molybdenum cluster exhibiting prominent photoactive
941 and oxidation properties. *Applied Clay Science*, 96 (2020) 105765.
942 <https://doi.org/10.1016/j.clay.2020.105765>

943 [53] T. K. N. Nguyen, B. Dierre, F. Grasset, A. Renaud, S. Cordier, P. Lemoine, N.
944 Ohashi, T. Uchikoshi, Formation Mechanism of Transparent Mo₆ Metal Atom Cluster
945 Film Prepared by Electrophoretic Deposition. *Journal of The Electrochemical Society*,
946 164 (2017) 412-418. <https://doi.org/10.1149/2.0591707jes>

947 [54] M. V. Marchuk, N. A. Vorotnikova, Y. A. Vorotnikov, N. V. Kuratieva, D. V. Stass,
948 and M. A. Shestopalov, Optical property trends in a family of {Mo₆I₈} aquahydroxo
949 complexes, *Dalton Trans.*, 2021, 50, 8794–8802. <https://doi.org/10.1039/D1DT01293B>
950 [55] J. Liu, J. Jin, Y. Li, H.W. Huang, C. Wang, M. Wu, L.-H. Chen and B.-L. Su, Tracing
951 the slow photon effect in a ZnO inverse opal film for photocatalytic activity enhancement,
952 *J. Mater. Chem. A*, 2 (2014) 5051–5059, DOI: 10.1039/c3ta15044e
953 [56] H. Zhao, Z. Hua, J.Liu, Y.Li, M.Wu, G. V. Tendeloo, B.-L. Suade, Blue-edge slow
954 photons promoting visible-light hydrogen production on gradient ternary 3DOM TiO₂-
955 Au-CdS photonic crystals, *Nano Energy*, 47 (2018) 266-274, DOI:
956 10.1016/j.nanoen.2018.02.052
957 [57] Z. Li, S. Feng, Y. Liu, J. Hu, C. Wang, B. Wei, Enhanced Tunable Light Absorption
958 In Nanostructured Si Arrays Based On Double-Quarter-Wavelength Resonance, *Adv.*
959 *Opt. Mater.*, 7 (2019) 1900845, DOI: 10.1002/adom.201900845
960 [58] N. A. Vorotnikova, Y. A. Vorotnikov, I. N. Novozhilov, M. M. Syrokvashin, V. A.
961 Nadolinny, N. V. Kuratieva, D. M. Benoit, Y. V. Mironov, R. I. Walton, G. I. Clarkson,
962 N.Kitamura, A. J. Sutherla, M. A. Shestopalov, P. A. Efremova, ²³-Electron Octahedral
963 Molybdenum Cluster Complex [{Mo₆I₈}Cl₆]⁻. *Inorg. Chem.*, 57 (2018) 811–820.
964 <https://doi.org/10.1021/acs.inorgchem.7b02760>
965 [59] P. Kumar, H.P. Mungse, S. Cordier, R. Boukherroub, O. P. Khatri, S. L. Jain,
966 Hexamolybdenum clusters supported on graphene oxide: Visible-light Induced
967 Photocatalytic Reduction of Carbon Dioxide Into Methanol. *Carbon*, 94 (2015) 91-100.
968 <https://doi.org/10.1016/j.carbon.2015.06.029>
969 [60] K. D. Kreuer, A. Rabenau, W. Weppner, Vehicle Mechanism, A New Model for The
970 Interpretation of The Conductivity of Fast Proton Conductors, *Angew. Chem. Int. Ed.*
971 *Engl.*, 21 (1982) 208-209. <https://doi.org/10.1002/anie.198202082>
972 [61] G. Daigre, J.Cuny, P. Lemoine, M. Amela-Cortes, S. Paofai, N.Audebrand, A. L. G.
973 L. Salle, E. Quarez, O.Joubert, N. G. Naumovand, S.Cordier, Metal Atom Clusters as
974 Building Blocks for Multifunctional Proton- Conducting Materials: Theoretical and
975 Experimental Characterization. *Inorg. Chem.*, 7 (2018), 814–9825.
976 <https://doi.org/10.1021/acs.inorgchem.8b00340>

977 [62] A. Barras, M. A. Das, R. R. Devarapalli, M. V. Shelke, S. Cordier, S. Szunerits, R.
978 Boukherroub, One-pot synthesis of gold nanoparticle/molybdenum cluster/graphene
979 oxide nanocomposite and its photocatalytic activity. *Appl. Catalysis B: Environmental*,
980 30–131 (2013) 70–276. <https://doi.org/10.1016/j.apcatb.2012.11.017>

981 [63] T. Aubert, F. Cabello-Hurtado, M. A. Esnault, C. Neaime, D. Le Bret-Chauvel, S.
982 Jeanne, P. Pellen, C. Roiland, L. L. Polles, N. Saito, K. Kimoto, H. Haneda, N. Ohashi,
983 F. Grasset, Extended Investigations on Luminescent Cs₂[Mo₆Br₁₄]/SiO₂ Nanoparticles:
984 Physico-Structural Characterizations and Toxicity Studies. *J. Phys. Chem. C*, 17 (2013)
985 20154–20163. <https://doi.org/10.1021/jp405836q>

986 [64] M. N. Ivanova, Y. A. Vorotnikov, E. E. Plotnikova, M. V. Marchuk, A. A. Ivanov,
987 A. A. Ivanov, I. P. Asanov, A. R. Tsygankova, E. D. Grayfer, V. E. Fedorov, M. A.
988 Shestopalov, Hexamolybdenum Clusters Supported on Exfoliated h BN Nanosheets for
989 Photocatalytic Water Purification. *Inorg. Chem.*, 9 (2020) 6439–6448.
990 <https://doi.org/10.1021/acs.inorgchem.0c00528>

991

992